LOW MACH NUMBER MODELING OF TYPE Ia SUPERNOVAE. III. REACTIONS

A. S. ALMGREN,[1] J. B. BELL,[1] A. NONAKA,[1] AND M. ZINGALE[2]

ABSTRACT

We continue the description of a low Mach number hydrodynamics algorithm for reacting, full star flows. Here we demonstrate how to accurately incorporate reactions using a second-order accurate Strang-splitting technique. We also improve the fidelity of the model by allowing the base state to evolve in response to large-scale convection as well as large-scale heating, taking care to account for the compositional changes to the base state as well. The new algorithm is tested via comparisons with a fully compressible code and shown to be in good agreement. The resulting code, MAESTRO, once extended to incorporate a spherically symmetric base state, will be used to study the convection and ignition phases of Type Ia supernovae.

Subject headings: convection — hydrodynamics — methods: numerical — nuclear reactions, nucleosynthesis, abundances — supernovae: general — white dwarfs

1. INTRODUCTION

In the generally accepted model of Type Ia supernovae (SNe Ia), a white dwarf accretes mass from a companion until it reaches the Chandrasehkar mass (see Hillebrandt & Niemeyer 2000 for a recent review). For centuries, subsonic convection (Mach number, M, ~0.01–0.1) transports heat generated at or near the center throughout the star (Baraffe et al. 2004; Woosley et al. 2004; Wunsch & Woosley 2004; Kuhlen et al. 2006). Only in the last second before the star unbinds does the Mach number approach, and possibly exceed, unity. It is the details of this convective phase that determine initial conditions for the subsequent explosion. Simulations have shown that different approximations for the initial conditions lead to very different explosion behaviors (Niemeyer et al. 1996; Plewa et al. 2004; García-Senz & Bravo 2005; Livne et al. 2005; Röpke et al. 2006, 2007). Efficient simulation of this convection requires modern numerical methods tuned to the conditions in the star. Other astrophysical environments, such as classical novae and X-ray bursts, are also characterized by low Mach number dynamics and could benefit from the algorithm approach outlined below.

In this paper we continue the development of a low Mach number hydrodynamics algorithm for astrophysical flows. As shown previously (see Almgren et al. 2006a, hereafter Paper I; Almgren et al. 2006b, hereafter Paper II), the low Mach number hydrodynamics system of equations accurately describes the typical flows in SNe Ia conditions for Mach numbers less than 0.2, providing a robust representation of finite-amplitude density and temperature perturbations and accurately capturing the expansion of the atmosphere due to heat release. Here we generalize the model from Paper II in two fundamental ways. First, we add species advection with realistic burning networks to the previous framework. Next, we modify the evolution equations to allow the base state to evolve in response to large-scale convective motions as well as heat release. In the next paper we will generalize the algorithm to spherical configurations. Here, we focus on planeparallel geometries in order to more carefully test the new aspects of the algorithm via straightforward comparison to compressible codes.

The traditional approach for modeling the time evolution of astrophysical flows uses a fully explicit time discretization of the compressible equation set (see, e.g., Fryxell et al. 2000). An alternative to this approach that is applicable for low Mach number flows is a fully implicit method for solving the compressible equation set. A recent example of this type of approach is found in Hujeirat et al. (2007), where an implicit solver based on nonlinear Newton-type solvers in combination with the defect-correction iteration procedure is introduced.

By contrast, our work, as well as recent work by Lin et al. (2006), reformulate the system analytically to generate a low Mach number equation set, which is then solved with a projection-type method. The method presented in Lin et al. (2006) is similar to that presented here, but with several key differences. First, their method does not allow for base state expansion and, therefore, is restricted to situations where the total energy release and large-scale convective motions are not sufficient to significantly alter the radially averaged state. In addition, the form in which the equations are solved numerically differs between the two algorithms. Low Mach number models, which include a constraint on the divergence of the velocity field, are typically integrated using a fractional step projection approach. In this approach, one first advances the system without satisfying the constraint. In the second step, a discrete projection is then applied so that the low Mach number divergence constraint is satisfied. With this type of fractional step approach it is not possible to numerically conserve mass and energy (or enthalpy) while simultaneously satisfying the equation of state. In Lin et al. (2006) the temperature is evolved and the equation of state is used to find the new density. Instead, we solve conservative equations for both density and enthalpy and relax the equation of state. The second major difference between our approach and that of Lin et al. relates to the projection step of the algorithm. Lin et al. formulate a projection algorithm in terms of a constant-coefficient pressure Poisson equation, derived from the mass conservation equation, to be solved at each time step. In contrast, we define the projection as an orthogonal decomposition of velocity in a weighted inner product space. While our approach leads to a somewhat more expensive variable-coefficient elliptic solve, it has the advantage that it can handle larger density contrasts without encountering stability issues (see Bell & Marcus 1992;

[1] Center for Computational Science and Engineering, Lawrence Berkeley National Laboratory, Berkeley, CA 94720.

[2] Department of Physics and Astronomy, SUNY Stony Brook, Stony Brook, NY 11794-3800.

Almgren et al. 1998; Sussman et al. 1999) and has been shown to have better convergence properties (see Nicoud 2000). Finally, our method is based on a second-order accurate discretization in space and time.

Our goal for the current algorithm is to simulate the convection that precedes the explosion of the white dwarf, in order to understand how ignition occurs. Other algorithms have been used in the literature to study this problem, including an implicit method (Höflich & Stein 2002) and the anelastic approximation (Kuhlen et al. 2006). Few details are provided about the implicit algorithm used by Höflich & Stein (2002), so it is difficult to compare it to our new algorithm. Direct comparisons with the anelastic method, presented in Paper I, showed that at low Mach numbers and small deviations of temperature and density from the background state, the low Mach number method and the anelastic method agree well. The low Mach number method continues to be valid for large density and temperature perturbations where the anelastic formulation breaks down. We plan to follow the evolution of the convection through the development of finite-amplitude hot spots, as well as capture the expansion of the white dwarf as it is heated by the reactions at the center.

In § 2 we discuss the low Mach number equation set with a reaction network. In § 3 the numerical methodology is explained in detail. Results are in § 4, including comparisons to a fully compressible code and convergence tests. We conclude in § 5.

2. LOW MACH NUMBER HYDRODYNAMICS

In Paper II we derived a system of low Mach number equations for stellar atmospheres with a time-dependent background state that depended on externally prescribed heat sources. In this paper we generalize the low Mach number equation set from Paper II to include reaction networks. The necessary assumption for validity of the generalized system is, as before, that the Mach number (M) of the flow be small. Then we can decompose the pressure, $p(\boldsymbol{x}, r, t)$, into a base state pressure, $p_0(r, t)$, and a perturbational, or dynamic, pressure, $\pi(\boldsymbol{x}, r, t)$, such that $|\pi|/p_0 = O(M^2)$. Here, $\boldsymbol{x}$ represents the horizontal coordinate directions, and r represents the radial direction. The perturbations of density and temperature need not be small. The base state is assumed to be in hydrostatic equilibrium, i.e., $\nabla p_0 = -\rho_0 g \boldsymbol{e}_r$, where $\rho_0 = \rho_0(r, t)$ is the base state density and $\boldsymbol{e}_r$ is the unit vector in the radial direction.

We recall from Paper I the fully compressible equations of motion in a stellar environment with species evolution equations and reaction terms,

$$\frac{\partial \rho}{\partial t} + \nabla \cdot (\rho \boldsymbol{U}) = 0, \tag{1}$$

$$\frac{\partial (\rho \boldsymbol{U})}{\partial t} + \nabla \cdot (\rho \boldsymbol{U} \boldsymbol{U}) + \nabla p = -\rho g \boldsymbol{e}_r, \tag{2}$$

$$\frac{\partial (\rho h)}{\partial t} + \nabla \cdot (\boldsymbol{U} \rho h) = \frac{Dp}{Dt} + \rho H_{\mathrm{nuc}} + \rho H_{\mathrm{ext}}, \tag{3}$$

$$\frac{\partial (\rho X_k)}{\partial t} + \nabla \cdot (\boldsymbol{U} \rho X_k) = \rho \dot{\omega}_k, \tag{4}$$

where ρ, $\boldsymbol{U}$, h, and p are the density, velocity, enthalpy, and pressure, respectively. Here we have written the energy equation in terms of enthalpy rather than total energy, as in Paper I. The species are represented by their mass fractions, X_k, along with their associated production rates, $\dot{\omega}_k$. Equations (1) and (4) for the mass and species are degenerate, since

$$\sum_k X_k = 1,$$

and therefore, by definition,

$$\sum_k \dot{\omega}_k = \frac{D}{Dt} \sum_k X_k = 0.$$

In the absence of weak interactions, the nuclear energy generation rate, H_{nuc} (expressed in erg g^{-1} s^{-1}), can be expressed in terms of the specific binding energies, q_k, as

$$H_{\mathrm{nuc}} = -\sum_k q_k \dot{\omega}_k. \tag{5}$$

This is the form we use in this paper. We note that neutrino losses can easily be added to this term as well. For generality we retain the external heat source, H_{ext}, from Paper II. For the plane-parallel applications in this paper, we take the gravitational acceleration, g, to be constant. Finally, the system is closed with the equation of state,

$$p = p(\rho, h, X_k).$$

As in Papers I and II we use a general, publicly available stellar equation of state based on the Helmholtz free energy, with contributions from ions, radiation, and electron degeneracy, as described in Timmes & Arnett (1999), Timmes & Swesty (2000), and Fryxell et al. (2000). For the calculations presented in this paper and in our previous small-scale flame calculations (Bell et al. 2004), we have not included Coulomb corrections. For the comparisons with the compressible method we set coulomb_mult to 0.0 in the FLASH code. However, we will include these contributions for our scientific investigations of full white dwarfs.

We now derive the low Mach number equation set in a manner analogous to the derivation in Paper II, but with species and reaction terms added. We rewrite conservation of mass as an expression for the divergence of velocity,

$$\nabla \cdot \boldsymbol{U} = -\frac{1}{\rho} \frac{D\rho}{Dt}. \tag{6}$$

Differentiating the equation of state, written in the form, $p = p(\rho, T, X_k)$, along particle paths, we can write

$$\frac{D\rho}{Dt} = \frac{1}{p_\rho} \left(\frac{Dp}{Dt} - p_T \frac{DT}{Dt} - \sum_k p_{X_k} \dot{\omega}_k \right), \tag{7}$$

with $p_\rho = \partial p / \partial \rho|_{X_k, T}$, $p_{X_k} = \partial p / \partial X_k|_{T, \rho, (X_j, j \neq k)}$, and $p_T = \partial p / \partial T|_{\rho, X_k}$.

An expression for DT/Dt can be found by applying the chain rule for $h = h(p, T, X_k)$ to the enthalpy equation (3),

$$\frac{DT}{Dt} = \frac{1}{\rho c_p} \left[\left(1 - \rho h_p \right) \frac{Dp}{Dt} - \sum_k \rho \xi_k \dot{\omega}_k + \rho H_{\mathrm{nuc}} + \rho H_{\mathrm{ext}} \right], \tag{8}$$

where $c_p = \partial h / \partial T|_{p, X_k}$ is the specific heat at constant pressure, $h_p \equiv \partial h / \partial p|_{T, X_k}$, and $\xi_k \equiv \partial h / \partial X_k|_{T, p, (X_j, j \neq k)}$ for convenience. Combining equations (6), (7), and (8) and replacing p by $p_0(r, t)$, we arrive at the divergence constraint on the velocity field,

$$\nabla \cdot \boldsymbol{U} + \alpha \left(\frac{\partial p_0}{\partial t} + \boldsymbol{U} \cdot \nabla p_0 \right)$$
$$= -\sigma \sum_k \xi_k \dot{\omega}_k + \frac{1}{\rho p_\rho} \sum_k p_{X_k} \dot{\omega}_k + \sigma H_{\mathrm{nuc}} + \sigma H_{\mathrm{ext}} \equiv S, \tag{9}$$

where

$$\alpha \equiv -\left[\frac{(1 - \rho h_p)p_T - \rho c_p}{\rho^2 c_p p_\rho}\right] = \frac{1}{\Gamma_1 p_0}, \qquad (10)$$

$\Gamma_1 \equiv d(\log p)/d(\log \rho)$ at constant entropy, and $\sigma \equiv p_T/(\rho c_p p_\rho)$. Here, we set $\Gamma_1 = \overline{\Gamma}_1$, where $\overline{\Gamma}_1$ is the lateral average of Γ_1, i.e.,

$$\overline{\Gamma}_1(r) = \frac{1}{A(\Omega_H)} \int_{\Omega_H} \Gamma_1(\boldsymbol{x}, r)\, dA, \qquad (11)$$

where $A(\Omega_H) \equiv \int_{\Omega_H} dA$, Ω_H is a region at constant height for the plane-parallel atmosphere, and dA represents an area measure. This is a departure from the construction in Papers I and II, where we used $\Gamma_{10} = \Gamma_1(\rho_0, p_0, X_{k0})$. The variation of Γ_1 is explored in the numerical tests presented in § 4.2 to ensure that the use of the averaged Γ_1 term is reasonable.

We note that the source term, S, is the same as that in our small-scale low Mach number astrophysical combustion algorithm (Bell et al. 2004), with the absence of thermal conduction and the addition of an explicit heating term. (We also note that we have changed our notation from Papers I and II from $\tilde{S}$ to S. This is consistent with Bell et al. [2004].) We recall from Papers I and II that this constraint can be written as

$$\nabla \cdot (\beta_0 \boldsymbol{U}) = \beta_0 \left(S - \alpha \frac{\partial p_0}{\partial t}\right), \qquad (12)$$

where

$$\beta_0(r, t) = \beta(0, t) \exp\left(\int_0^r \frac{1}{\overline{\Gamma}_1 p_0} \frac{\partial p_0}{\partial r'}\, dr'\right). \qquad (13)$$

Summarizing the reacting low Mach number equation set, we have

$$\frac{\partial(\rho X_k)}{\partial t} = -\nabla \cdot (\boldsymbol{U} \rho X_k) + \rho \dot{\omega}_k, \qquad (14)$$

$$\frac{\partial(\rho h)}{\partial t} = -\nabla \cdot (\boldsymbol{U} \rho h) + \frac{Dp_0}{Dt} + \rho H_{\text{nuc}} + \rho H_{\text{ext}}, \qquad (15)$$

$$\frac{\partial \boldsymbol{U}}{\partial t} = -\boldsymbol{U} \cdot \nabla \boldsymbol{U} - \frac{1}{\rho} \nabla \pi - \frac{(\rho - \rho_0)}{\rho} g \boldsymbol{e}_r, \qquad (16)$$

$$\nabla \cdot (\beta_0 \boldsymbol{U}) = \beta_0 \left(S - \frac{1}{\overline{\Gamma}_1 p_0} \frac{\partial p_0}{\partial t}\right), \qquad (17)$$

where the total mass density is defined as

$$\rho = \sum_k \rho X_k, \qquad (18)$$

and S is given by

$$S = -\sigma \sum_k \xi_k \dot{\omega}_k + \frac{1}{\rho p_\rho} \sum_k p_{X_k} \dot{\omega}_k + \sigma H_{\text{nuc}} + \sigma H_{\text{ext}}. \qquad (19)$$

The major difference in the constraint considered in this paper relative to Paper II is the form of S. Now, in addition to the external heat source, there is a reaction heat source (the H_{nuc} term) and compressibility terms due solely to compositional changes (the terms proportional to ξ_k and p_{X_k}). Here, $\dot{\omega}_k$ is evaluated by integrating the reaction network. The thermodynamic derivatives with respect to X_k are discussed in Appendix A.

An underlying assumption in the low Mach number approximation is that the pressure remains close to the background pressure. Heat release from reactions and large-scale convective motions in a convectively unstable background can both cause the background state to evolve in time. As discussed in Almgren (2000) and demonstrated numerically in Paper II for an externally specified heating profile, if the base state does not evolve in response to heating, the low Mach number method quickly becomes invalid.

We recall from Paper II that we can decompose the full velocity field, $\boldsymbol{U}$, into a base state velocity, $w_0 \boldsymbol{e}_r$, and the remaining velocity field, $\tilde{\boldsymbol{U}}$, that governs the more local dynamics, i.e.,

$$\boldsymbol{U}(\boldsymbol{x}, r, t) = w_0(r, t)\boldsymbol{e}_r + \tilde{\boldsymbol{U}}(\boldsymbol{x}, r, t). \qquad (20)$$

The decomposition is uniquely determined by the requirement that

$$\int_{\Omega_H} \tilde{\boldsymbol{U}} \cdot \boldsymbol{e}_r\, dA = 0, \qquad (21)$$

which defines

$$w_0 = \frac{1}{A(\Omega_H)} \int_{\Omega_H} (\boldsymbol{U} \cdot \boldsymbol{e}_r)\, dA. \qquad (22)$$

Following Paper II we can separate the divergence constraint into that governing $\tilde{\boldsymbol{U}}$ and that governing w_0, resulting in the expression

$$\nabla \cdot (\beta_0 w_0 \boldsymbol{e}_r) = \beta_0 \left(\overline{S} - \frac{1}{\overline{\Gamma}_1 p_0} \frac{\partial p_0}{\partial t}\right), \qquad (23)$$

with

$$\overline{S}(r) = \frac{1}{A(\Omega_H)} \int_{\Omega_H} S\, dA. \qquad (24)$$

In Paper II, given w_0, we updated the base state pressure and density using

$$\frac{\partial p_0}{\partial t} = -w_0 \frac{\partial p_0}{\partial r}, \qquad (25)$$

$$\frac{\partial \rho_0}{\partial t} = -\nabla \cdot (\rho_0 w_0 \boldsymbol{e}_r). \qquad (26)$$

While these evolution equations preserve hydrostatic equilibrium of the base state and allow expansion of the base state due to nonzero $\overline{S}$, they neglect base state changes that could occur due to significant convective overturning. To quantify this effect, we first define $\rho' = \rho - \rho_0$. Using this definition and the velocity decomposition equation (20), the evolution of ρ' can be written by subtracting equation (26) from equation (1),

$$\frac{\partial \rho'}{\partial t} = -\nabla \cdot (\rho_0 \tilde{\boldsymbol{U}}) - \nabla \cdot (\rho' w_0 \boldsymbol{e}_r) - \nabla \cdot (\rho' \tilde{\boldsymbol{U}}). \qquad (27)$$

The horizontal average of each of the first two terms on the right-hand side of equation (27) is zero, but the average of the third term, in general, is not. Consequently, $\overline{\rho'}$, the horizontal average of ρ', can change over time. In particular,

$$\frac{\partial}{\partial t} \overline{\rho'} = -\frac{\partial}{\partial r} \overline{(\rho' \tilde{w})}, \qquad (28)$$

where $\tilde{w} = \tilde{\boldsymbol{U}} \cdot \boldsymbol{e}_r$.

In the algorithm as presented in Paper II, the nonzero right-hand side in equation (28) allowed the base state density and average density to gradually drift apart. As a result, the base state pressure could also drift away from hydrostatic balance determined from the average density. For the nearly isentropically stratified flows considered in that paper, this drift is negligible. However, in a more general case where there is significant convective overturning or when reactions produce significant changes in composition, this effect can lead to a loss of physical fidelity over time.

In this paper we correct for this drift from the average. We retain our velocity decomposition, but alter the base state evolution equations. Guided by equation (28), we replace equation (26) by

$$\frac{\partial \rho_0}{\partial t} = -\nabla \cdot (\rho_0 w_0 \boldsymbol{e}_r) - \nabla \cdot (\eta_\rho \boldsymbol{e}_r), \qquad (29)$$

where we define

$$\eta_\rho(r) = \overline{(\rho' \tilde{w})} = \frac{1}{A(\Omega_H)} \int_{\Omega_H} (\rho' \tilde{w}) \, dA. \qquad (30)$$

This has the consequence that if $\overline{\rho'} = 0$ at $t = 0$, then $\overline{\rho'} = 0$ for all time.

We can derive the base state pressure evolution directly from the hydrostatic balance equation. Starting with the equation of hydrostatic equilibrium, $\partial p_0 / \partial r = -\rho_0 g$, and using the new base state density equation (29), one can show that in the case of plane-parallel geometry with constant gravity, g, the base state pressure is governed by

$$\frac{\partial p_0}{\partial t} = w_0 \rho_0 g + \eta_\rho g = -w_0 \frac{\partial p_0}{\partial r} + \eta_\rho g. \qquad (31)$$

We define the Lagrangian change in the base state pressure as

$$\psi \equiv \frac{D_0 p_0}{Dt}, \qquad (32)$$

where $D_0/Dt \equiv \partial/\partial t + w_0 \, \partial/\partial r$. Note that for plane-parallel geometries, equation (31) can also be written as $\psi = \eta_\rho g$. The evolution equation for p_0 in spherical coordinates will be discussed in a forthcoming paper. With this definition, we can write the full enthalpy equation (eq. [3]) as

$$\frac{\partial(\rho h)}{\partial t} + \nabla \cdot (\boldsymbol{U} \rho h) = \psi + (\tilde{\boldsymbol{U}} \cdot \boldsymbol{e}_r) \frac{\partial p_0}{\partial r} + \rho H_{\text{nuc}} + \rho H_{\text{ext}} \qquad (33)$$

and the temperature evolution equation (eq. [8]) as

$$\frac{DT}{Dt} = \frac{1}{\rho c_p} \left\{ (1 - \rho h_p) \left[\psi + (\tilde{\boldsymbol{U}} \cdot \boldsymbol{e}_r) \frac{\partial p_0}{\partial r} \right] \right. $$
$$\left. - \sum_k \rho \xi_k \dot{\omega}_k + \rho H_{\text{nuc}} + \rho H_{\text{ext}} \right\}. \qquad (34)$$

In Paper II we also defined an evolution equation for the base state enthalpy, so that we could construct the fluxes used in the enthalpy evolution equation in perturbational form. Numerical experiments conducted later indicated that an alternate formulation, described below in this paper, had better numerical properties, although analytically equivalent. Thus, we no longer utilize a base state enthalpy or base state species concentration; only the base state density and pressure are essential to the low Mach number formulation.

Finally, we use equations (23) and (31) to define w_0. In plane-parallel geometry,

$$\frac{\partial w_0}{\partial r} = \frac{1}{\beta_0} \nabla \cdot (\beta_0 w_0 \boldsymbol{e}_r) - w_0 \frac{1}{\beta_0} \frac{\partial \beta_0}{\partial r}$$
$$= \left(\overline{S} - \frac{1}{\overline{\Gamma}_1 p_0} \frac{\partial p_0}{\partial t} \right) - w_0 \frac{1}{\beta_0} \frac{\partial \beta_0}{\partial r}$$
$$= \overline{S} - \frac{1}{\overline{\Gamma}_1 p_0} \left(\frac{\partial p_0}{\partial t} + w_0 \frac{\partial p_0}{\partial r} \right)$$
$$= \overline{S} - \frac{1}{\overline{\Gamma}_1 p_0} \eta_\rho g, \qquad (35)$$

where we have used $(\overline{\Gamma}_1 p_0)^{-1}(\partial p_0 / \partial r) = \beta_0^{-1}(\partial \beta_0 / \partial r)$, as shown in Paper I. A different constraint equation for w_0 would be needed for spherical coordinates.

In writing the evolution of the velocity field, we make a slight correction to the evolution equation for $\tilde{\boldsymbol{U}}$ given in Paper II, equation (23). There we incorrectly split the dynamics between $\tilde{\boldsymbol{U}}$ and w_0; in effect, we neglected the perturbational pressure term that appears in the evolution of w_0. Here, after correctly splitting the dynamics, we now have

$$\frac{\partial w_0}{\partial t} = -w_0 \frac{\partial w_0}{\partial r} - \frac{1}{\rho_0} \frac{\partial \pi_0}{\partial r}, \qquad (36)$$

$$\frac{\partial \tilde{\boldsymbol{U}}}{\partial t} = -\tilde{\boldsymbol{U}} \cdot \nabla \tilde{\boldsymbol{U}} - w_0 \frac{\partial \tilde{\boldsymbol{U}}}{\partial r} - (\tilde{\boldsymbol{U}} \cdot \boldsymbol{e}_r) \frac{\partial w_0}{\partial r} \boldsymbol{e}_r$$
$$- \frac{1}{\rho} \nabla \pi + \frac{1}{\rho_0} \frac{\partial \pi_0}{\partial r} \boldsymbol{e}_r - \frac{(\rho - \rho_0)}{\rho} g \boldsymbol{e}_r, \qquad (37)$$

where we have introduced a new term, $(1/\rho_0)(\partial \pi_0 / \partial r)$, that contributes to the change in w_0. We note that without this term in equation (36), an initially zero w_0 would remain zero for all time. Similarly to π, the magnitude of π_0 is such that $|\pi_0|/|p_0| = O(M_0^2)$, where $M_0 = |w_0|/c$, so we can neglect its effect on thermodynamic relations.

In practice, we calculate w_0 by integrating the one-dimensional divergence constraint (see eq. [35]). Then we define

$$-\frac{1}{\rho_0} \frac{\partial \pi_0}{\partial r} = \frac{\partial w_0}{\partial t} + w_0 \frac{\partial w_0}{\partial r}, \qquad (38)$$

once w_0 at the old and new times is known, and the advective term is computed explicitly. Then we can include this for completeness in the update for $\tilde{\boldsymbol{U}}$. The constraint equation for $\tilde{\boldsymbol{U}}$ remains as in Paper II,

$$\nabla \cdot (\beta_0 \tilde{\boldsymbol{U}}) = \beta_0 (S - \overline{S}). \qquad (39)$$

3. NUMERICAL METHODOLOGY

The numerical methodology in this paper is more complicated than that outlined in Paper II because of the need to integrate the reaction network. Again, we use a predictor-corrector formalism. In the predictor step we compute an estimate of the expansion of the base state, then compute an estimate of the state at the new time level. In the corrector step we use the results of the previous state update to compute a new base state update as well as full state update. We include the reactions using Strang-splitting to achieve second-order accuracy in time.

3.1. *Notation*

We make use of the following shorthand notations in outlining the algorithm.

1. For any quantity, ϕ, we define $\overline{\phi} = \text{Avg}(\phi)$, the average over Ω_H, as

$$\overline{\phi}(r) = \frac{1}{A(\Omega_H)} \int_{\Omega_H} \phi(r, \boldsymbol{x}) \, dA. \tag{40}$$

2. React State$[\rho^{\text{in}}, (\rho h)^{\text{in}}, X_k^{\text{in}}, T^{\text{in}}, (\rho H_{\text{ext}})^{\text{in}}] \rightarrow [\rho^{\text{out}}, (\rho h)^{\text{out}}, X_k^{\text{out}}, T^{\text{out}}, (\rho \dot{\omega}_k)^{\text{out}}]$ is the process by which we evolve the species and enthalpy from $X_k^{\text{in}} \rightarrow X_k^{\text{out}}$ and $(\rho h)^{\text{in}} \rightarrow (\rho h)^{\text{out}}$ by solving the following system of equations over a time interval of $\Delta t/2$,

$$\frac{\partial X_k}{\partial t} = \dot{\omega}_k, \tag{41}$$

$$\frac{\partial (\rho h)}{\partial t} = \rho H_{\text{nuc}} + \rho H_{\text{ext}}. \tag{42}$$

In particular, to evolve the species, we solve the system

$$\frac{dX_k}{dt} = \dot{\omega}_k(\rho, X_k, T), \tag{43}$$

$$\frac{dT}{dt} = \frac{1}{c_p} \left(-\sum_k \xi_k \dot{\omega}_k + H_{\text{nuc}} \right), \tag{44}$$

using the stiff ordinary differential equation integration methods provided by the VODE package (Brown et al. 1989). The absolute error tolerances are set to 10^{-12} for the species, and a relative tolerance of 10^{-5} is used for the temperature. The integration yields the new values of the mass fractions, X_k^{out}. Equation (44) is derived from equation (8) by assuming that the pressure is constant during the burn state. In evolving these equations, we need to evaluate c_p and ξ_k. In theory, this means evaluating the equation of state for each right-hand side evaluation that VODE requires. In practice, we freeze c_p and ξ_k at the start of the integration time step and compute them using ρ^{in}, X_k^{in}, and T^{in} as inputs to the equation of state. We note that while temperature is evolved when solving these equations, we do not keep the final temperature, nor do we use it to compute the final change in enthalpy. Therefore, $T^{\text{out}} = T^{\text{in}}$. Also, note that the density remains unchanged during the React State step, i.e., $\rho^{\text{out}} = \rho^{\text{in}}$.

After the new mass fractions have been computed, the reaction rates are defined as

$$(\rho \dot{\omega}_k)^{\text{out}} = \frac{\rho^{\text{out}} \left(X_k^{\text{out}} - X_k^{\text{in}} \right)}{\Delta t/2}, \tag{45}$$

and the nuclear energy generation rate is defined as

$$(\rho H_{\text{nuc}}) = -\sum_k (\rho \dot{\omega}_k)^{\text{out}} q_k. \tag{46}$$

The enthalpy update incorporates the external heating, $(\rho H_{\text{ext}})^{\text{in}}$, and is updated by

$$(\rho h)^{\text{out}} = (\rho h)^{\text{in}} + \frac{\Delta t}{2} (\rho H_{\text{nuc}}) + \frac{\Delta t}{2} (\rho H_{\text{ext}})^{\text{in}}. \tag{47}$$

3. Advect Base$(\rho_0^{\text{in}}, p_0^{\text{in}}, \beta_0^{\text{in}}, w_0^{\text{in}}, \psi^{\text{in}}) \rightarrow (\rho_0^{\text{out}}, \rho_0^{\text{out}, n+1/2}, p_0^{\text{out}})$ is the process by which we update the base state through Δt in

time given the radial velocity w_0^{in}. Here we discuss the algorithm for plane-parallel geometries. The base state arrays are all one-dimensional in the radial coordinate; we think of the base state quantities as defined at cell centers, with w_0 and β_0 defined halfway in-between.

a) For the density update, we discretize equation (29), neglecting the η_ρ term, to compute the new base state density,

$$\rho_{0,j}^{\text{out}} = \rho_{0,j}^{\text{in}} - \frac{\Delta t}{\Delta r} \left[\left(\rho_0^{\text{out}, n+1/2} w_0^{\text{in}} \right)_{j+1/2} - \left(\rho_0^{\text{out}, n+1/2} w_0^{\text{in}} \right)_{j-1/2} \right],$$

where j refers to the one-dimensional index in the radial direction. The interface states, $\rho_0^{\text{out}, n+1/2}$, are found via the procedure described in Paper II, Appendix A, and are saved for use later in the overall algorithm.

b) For the pressure update, we discretize equation (31) to compute the new base state pressure,

$$p_{0,j}^{\text{out}} = p_{0,j}^{\text{in}} - \frac{\Delta t}{2\Delta r} \left(w_{0, j+1/2}^{\text{in}} + w_{0, j-1/2}^{\text{in}} \right)$$
$$\times \left(p_{0, j+1/2}^{n+1/2} - p_{0, j-1/2}^{n+1/2} \right) + \Delta t \psi_j^{\text{in}}, \tag{48}$$

where the interface states are again found via the procedure described in Paper II, Appendix A.

4. Correct Base$(\rho_0^{\text{in}}, \eta_\rho^{\text{in}}) \rightarrow (\rho_0^{\text{out}})$ is the process by which we adjust the base state density given η_ρ using

$$\rho_{0,j}^{\text{out}} = \rho_{0,j}^{\text{in}} - \frac{\Delta t}{\Delta r} \left(\eta_{\rho, j+1/2}^{\text{in}} - \eta_{\rho, j-1/2}^{\text{in}} \right). \tag{49}$$

3.2. *Time Advancement Algorithm*

We now describe the full time advancement algorithm, making frequent use of the shorthand developed above. Here, we assume that the problem is already properly initialized. We describe the details of the initialization in § 3.3.

In Paper II we discretized the density and enthalpy evolution equations in perturbational form, arguing that this would be less susceptible to grid effects. In the present algorithm, the analog would be to use a perturbational form of the species equations. Numerical testing has shown that the form of the algorithm presented here is in fact more robust than the perturbational form when the base state mixing terms (η_ρ) are included. In the algorithm described below, density is still extrapolated to edges in perturbational form, but we treat X_k and h in nonperturbational form.

STEP 1. *Define the average expansion at time $t^{n+1/2}$ and the new w_0.*

a) At the beginning of each time step, we need an estimate for the time-centered source term in the velocity divergence constraint (see eq. [9]). If this is the first step of the calculation ($n = 0$), we set

$$S^{1/2,\star} = \frac{S^0 + S^1}{2},$$

where S^1 is found through the iterative process that initializes the calculation. Otherwise, following the method used in our small-scale low Mach number algorithm (Bell et al. 2004), we

extrapolate to the half-time using the source terms at the previous and current time levels,

$$S^{n+1/2,\star} = S^n + \frac{\Delta t^n}{2} \frac{S^n - S^{n-1}}{\Delta t^{n-1}}. \tag{50}$$

b) Define

$$\overline{S}^{n+1/2,\star} = \mathrm{Avg}\left(S^{n+1/2,\star}\right).$$

c) Construct $w_0^{n+1/2,\star}$ by integrating equation (35) using the lagged $\psi^{n-1/2}$,

$$\frac{\partial w_0^{n+1/2,\star}}{\partial r} = \overline{S}^{n+1/2,\star} - \frac{1}{\overline{\Gamma}_1^n p_0^n} \psi^{n-1/2}. \tag{51}$$

For spherical geometries, this equation would be modified.

d) Using equation (38), define the scaled pressure gradient

$$-\left(\frac{1}{\rho_0^n} \frac{\partial \pi_0^{(1)}}{\partial r}\right) = \frac{w_0^{n+1/2,\star} - w_0^{n-1/2}}{(\Delta t^n + \Delta t^{n-1})/2} + w_0^{n,\star} \left(\frac{\partial w_0}{\partial r}\right)^{n,\star}, \tag{52}$$

where $w_0^{n,\star}$ and $(\partial w_0/\partial r)^{n,\star}$ are

$$w_0^{n,\star} = \frac{\Delta t^n w_0^{n-1/2} + \Delta t^{n-1} w_0^{n+1/2,\star}}{\Delta t^n + \Delta t^{n-1}}, \tag{53}$$

$$\left(\frac{\partial w_0}{\partial r}\right)^{n,\star} = \frac{1}{\Delta t^n + \Delta t^{n-1}} \left[\Delta t^n \left(\frac{\partial w_0}{\partial r}\right)^{n-1/2} + \Delta t^{n-1} \left(\frac{\partial w_0}{\partial r}\right)^{n+1/2,\star}\right]. \tag{54}$$

If $n = 0$, we use $\Delta t^{-1} = \Delta t^0$.

STEP 2. *Construct the provisional edge-based advective velocity,* $\tilde{U}^{\mathrm{ADV},(1)}$. The procedure to construct $\tilde{U}^{\mathrm{ADV},(1)}$ is described in detail in Appendix B. We note that $\tilde{U}^{\mathrm{ADV},(1)}$ satisfies the discrete versions of equations (21) and (39), in particular,

$$\nabla \cdot \left(\beta_0^n \tilde{U}^{\mathrm{ADV},(1)}\right) = \beta_0^n \left(S^{n+1/2,\star} - \overline{S}^{n+1/2,\star}\right). \tag{55}$$

STEP 3. *React the full state through the first time interval of* $\Delta t/2$.

a) React State $[\rho^n, (\rho h)^n, X_k^n, T^n, (\rho^n H_{\mathrm{ext}})] \rightarrow [\rho^{(1)}, (\rho h)^{(1)}, X_k^{(1)}, T^{(1)}, (\rho \dot{\omega}_k)^{(1)}]$.

b) Define

$$\overline{\Gamma}_1^{(1)} = \mathrm{Avg}\left[\Gamma_1(\rho^{(1)}, p_0^n, X_k^{(1)})\right],$$
$$\beta_0^{(1)} = \beta\left(\rho_0^n, p_0^n, \overline{\Gamma}_1^{(1)}\right). \tag{56}$$

STEP 4. *Advect the base state, then the full state, through a time interval of* Δt.

a) Advect Base $(\rho_0^n, p_0^n, \beta_0^{(1)}, w_0^{n+1/2,\star}, \psi^{n-1/2}) \rightarrow (\rho_0^{(2),\star}, \rho_0^{n+1/2,\star,\mathrm{pred}}, p_0^{n+1,\star})$.

b) Compute the edge states, $(\rho X_k)^{(1),n+1/2,\star}$ and $(\rho h)^{(1),n+1/2,\star}$, for the conservative update of (ρX_k) and (ρh). Here we predict ρ', T, and X_k to the edges, using a second-order Taylor expansion in space and time, as described in Paper II, Appendix A, using $V = \tilde{U}^{\mathrm{ADV},(1)} + w_0^{n+1/2,\star} e_r$. We explicitly include the reaction

terms in the temperature prediction, since we did not update the temperature in React State. We use the equation of state and base state density, ρ_0, to convert these to edge states for (ρX_k) and (ρh). We define $\rho^{(1),n+1/2,\star} = \sum_k (\rho X_k)^{(1),n+1/2,\star}$.

c) Evolve $(\rho X_k)^{(1)} \rightarrow (\rho X_k)^{(2),\star}$ and $(\rho h)^{(1)} \rightarrow (\rho h)^{(2),\star}$ without explicitly including the reaction terms,

$$(\rho X_k)^{(2),\star} = (\rho X_k)^{(1)} - \Delta t \times \left\{\nabla \cdot \left[\left(\tilde{U}^{\mathrm{ADV},(1)} + w_0^{n+1/2,\star} e_r\right)(\rho X_k)^{(1),n+1/2,\star}\right]\right\}, \tag{57}$$

$$(\rho h)^{(2),\star} = (\rho h)^{(1)} - \Delta t \left\{\nabla \cdot \left[\left(\tilde{U}^{\mathrm{ADV},(1)} + w_0^{n+1/2,\star} e_r\right) \times (\rho h)^{(1),n+1/2,\star}\right]\right\} + \Delta t (\tilde{U}^{\mathrm{ADV},(1)} \cdot e_r)\left(\frac{\partial p_0}{\partial r}\right)^n + \Delta t \psi^{n-1/2}, \tag{58}$$

$$\rho^{(2),\star} = \sum_k (\rho X_k)^{(2),\star}, \tag{59}$$

$$X_k^{(2),\star} = (\rho X_k)^{(2),\star}/\rho^{(2),\star}, \tag{60}$$

$$T^{(2),\star} = T\left(\rho^{(2),\star}, (\rho h)^{(2),\star}, X_k^{(2),\star}\right) \tag{61}$$

using the equation of state.

d) Correct Base $(\rho_0^{(2),\star}, \eta_\rho^{n-1/2}) \rightarrow (\rho_0^{n+1,\star})$.

e) Define an edge-centered $\eta_\rho^{n+1/2,\star}$ and cell-centered $\psi_j^{n+1/2,\star}$,

$$\eta_\rho^{n+1/2,\star} = \mathrm{Avg}\left[\left(\tilde{U}^{\mathrm{ADV},(1)} \cdot e_r + w_0^{n+1/2,\star}\right)\rho^{(1),n+1/2,\star}\right] - w_0^{n+1/2,\star} \rho_0^{n+1/2,\star,\mathrm{pred}},$$
$$\psi_j^{n+1/2,\star} = \frac{1}{2}\left(\eta_{\rho,j-1/2}^{n+1/2,\star} + \eta_{\rho,j+1/2}^{n+1/2,\star}\right)g. \tag{62}$$

For spherical geometries, $\psi_j^{n+1/2,\star}$ would have a different form.

STEP 5. *React the full state through a second time interval of* $\Delta t/2$.

a) React State $[\rho^{(2),\star}, (\rho h)^{(2),\star}, X_k^{(2),\star}, T^{(2),\star}, (\rho^{(2),\star} H_{\mathrm{ext}})] \rightarrow [\rho^{n+1,\star}, (\rho h)^{n+1,\star}, X_k^{n+1,\star}, T^{n+1,\star}, (\rho \dot{\omega}_k)^{(2),\star}]$.

b) Define

$$\overline{\Gamma}_1^{n+1,\star} = \mathrm{Avg}\left[\Gamma_1\left(\rho^{n+1,\star}, p_0^{n+1,\star}, X_k^{n+1,\star}\right)\right],$$
$$\beta_0^{n+1,\star} = \beta\left(\rho_0^{n+1,\star}, p_0^{n+1,\star}, \overline{\Gamma}_1^{n+1,\star}\right). \tag{63}$$

STEP 6. *Define a new average expansion rate at time* $t^{n+1/2}$.

a) Define

$$S^{n+1,\star} = -\sigma \sum_k \xi_k (\dot{\omega}_k)^{(2),\star} + \sigma H_{\mathrm{nuc}}^{(2),\star} + \frac{1}{\rho p_\rho} \sum_k p_{X_k} (\dot{\omega}_k)^{(2),\star} + \sigma H_{\mathrm{ext}}, \tag{64}$$

where $(\dot{\omega}_k)^{(2),\star} = (\rho \dot{\omega}_k)^{(2),\star}/\rho^{(2),\star}$ and the remaining quantities are defined using $X_k^{n+1,\star}$, $\rho^{n+1,\star}$, and $T^{n+1,\star}$ from step 5. Then define

$$S^{n+1/2} = \frac{S^n + S^{n+1,\star}}{2}.$$

b) Define

$$\overline{S}^{n+1/2} = \mathrm{Avg}\left(S^{n+1/2}\right).$$

c) Construct $w_0^{n+1/2}$ by integrating equation (35),

$$\frac{\partial w_0^{n+1/2}}{\partial r} = \overline{S}^{n+1/2,\star} - \frac{1}{\overline{\Gamma}_1^{n+1/2,\star} p_0^{n+1/2,\star}} \psi^{n+1/2,\star}, \quad (65)$$

for plane-parallel geometries, where $\overline{\Gamma}_1^{n+1/2,\star} = (\overline{\Gamma}_1^n + \overline{\Gamma}_1^{n+1,\star})/2$ and $p_0^{n+1/2,\star} = (p_0^n + p_0^{n+1,\star})/2$.

d) Using equation (38), define

$$-\left(\frac{1}{\rho_0^n}\frac{\partial \pi_0^{(2)}}{\partial r}\right) = \frac{w_0^{n+1/2} - w_0^{n-1/2}}{(1/2)(\Delta t^n + \Delta t^{n-1})} + w_0^n\left(\frac{\partial w_0}{\partial r}\right)^n, \quad (66)$$

where w_0^n and $(\partial w_0/\partial r)^n$ are defined analogously to equations (53) and (54).

STEP 7. *Construct the final edge-based advective velocity,* $\tilde{U}^{\text{ADV},(2)}$. The procedure to construct $\tilde{U}^{\text{ADV},(2)}$ is described in detail in Appendix B and is analogous to the procedure used in step 2, but with updated values for w_0 and π_0. We note that $\tilde{U}^{\text{ADV},(2)}$ satisfies the discrete versions of equations (21) and (39), in particular,

$$\nabla \cdot \left(\beta_0^{n+1/2,\star} \tilde{U}^{\text{ADV},(2)}\right) = \beta_0^{n+1/2,\star}\left(S^{n+1/2} - \overline{S}^{n+1/2}\right), \quad (67)$$

where $\beta_0^{n+1/2,\star} = (\beta_0^n + \beta_0^{n+1,\star})/2$.

STEP 8. *Advect the base state, then the full state, through a time interval of* Δt.

a) Advect Base $(\rho_0^n, p_0^n, \beta_0^{(1)}, w_0^{n+1/2}, \psi^{n+1/2,\star}) \rightarrow (\rho_0^{(2)}, \rho_0^{n+1/2,\text{pred}}, p_0^{n+1})$.

b) Compute the edge states, $(\rho X_k)^{(1),n+1/2}$ and $(\rho h)^{(1),n+1/2}$, for the conservative update of (ρX_k) and (ρh). Here we predict ρ', T, and X_k to the edges, using a second-order Taylor expansion in space and time, as described in Paper II, Appendix A, using $V = \tilde{U}^{\text{ADV},(2)} + w_0^{n+1/2}e_r$. Again, we explicitly include the reaction terms in the temperature prediction, since we did not update the temperature in React State. We use the equation of state and base state density, ρ_0, to convert these to edge states for (ρX_k) and (ρh). We define $\rho^{(1),n+1/2} = \sum_k (\rho X_k)^{(1),n+1/2}$.

c) Evolve $(\rho X_k)^{(1)} \rightarrow (\rho X_k)^{(2)}$ and $(\rho h)^{(1)} \rightarrow (\rho h)^{(2)}$,

$$(\rho X_k)^{(2)} = (\rho X_k)^{(1)} - \Delta t\Big\{\nabla \cdot \Big[\Big(\tilde{U}^{\text{ADV},(2)} + w_0^{n+1/2}e_r\Big)(\rho X_k)^{(1),n+1/2}\Big]\Big\}, \quad (68)$$

$$(\rho h)^{(2)} = (\rho h)^{(1)} - \Delta t\Big\{\nabla \cdot \Big[\Big(\tilde{U}^{\text{ADV},(2)} + w_0^{n+1/2}e_r\Big) \times (\rho h)^{(1),n+1/2}\Big]\Big\} + \frac{\Delta t}{2}\big(\tilde{U}^{\text{ADV},(2)} \cdot e_r\big) \times \left[\left(\frac{\partial p_0}{\partial r}\right)^n + \left(\frac{\partial p_0}{\partial r}\right)^{n+1}\right] + \Delta t\psi^{n+1/2,\star}, \quad (69)$$

$$\rho^{(2)} = \sum_k (\rho X_k)^{(2)}, \quad (70)$$

$$X_k^{(2)} = (\rho X_k)^{(2)}/\rho^{(2)}, \quad (71)$$

$$T^{(2)} = T\Big(\rho^{(2)}, (\rho h)^{(2)}, X_k^{(2)}\Big) \quad (72)$$

using the equation of state.

d) Correct Base$(\rho_0^{(2)}, \eta_\rho^{n+1/2,\star}) \rightarrow (\rho_0^{n+1})$.

e) Define an edge-centered $\eta_\rho^{n+1/2}$ and a cell-centered $\psi_j^{n+1/2}$,

$$\eta_\rho^{n+1/2} = \text{Avg}\Big[\Big(\tilde{U}^{\text{ADV},(2)} \cdot e_r + w_0^{n+1/2}\Big)\rho^{(1),n+1/2}\Big] - w_0^{n+1/2}\rho_0^{n+1/2,\text{pred}},$$

$$\psi_j^{n+1/2} = \frac{1}{2}\Big(\eta_{\rho, j-1/2}^{n+1/2} + \eta_{\rho, j+1/2}^{n+1/2}\Big)g. \quad (73)$$

STEP 9. *React the full state through a second time interval of* $\Delta t/2$.

a) React State $[\rho^{(2)}, (\rho h)^{(2)}, X_k^{(2)}, T^{(2)}, (\rho^{(2)}H_{\text{ext}})] \rightarrow [\rho^{n+1}, (\rho h)^{n+1}, X_k^{n+1}, T^{n+1}, (\rho\dot{\omega}_k)^{(2)}]$.

b) Define

$$\overline{\Gamma}_1^{n+1} = \text{Avg}\big[\Gamma_1\big(\rho^{n+1}, p_0^{n+1}, X_k^{n+1}\big)\big],$$

$$\beta_0^{n+1} = \beta\Big(\rho_0^{n+1}, p_0^{n+1}, \overline{\Gamma}_1^{n+1}\Big). \quad (74)$$

STEP 10. *Compute* S^{n+1} *for the final projection.*

a) Define

$$S^{n+1} = -\sigma\sum_k \xi_k(\dot{\omega}_k)^{(2)} + \sigma H_{\text{nuc}}^{(2)} + \frac{1}{\rho p_\rho}\sum_k p_{X_k}(\dot{\omega}_k)^{(2)} + \sigma H_{\text{ext}}, \quad (75)$$

where $(\dot{\omega}_k)^{(2)} = (\rho\dot{\omega}_k)^{(2)}/\rho^{(2)}$ and the remaining quantities are defined using X_k^{n+1}, ρ^{n+1}, and T^{n+1} from step 9.

b) Define

$$\overline{S}^{n+1} = \text{Avg}\big(S^{n+1}\big).$$

STEP 11. *Update the velocity.* The velocity update happens analogously to Paper II, using S^{n+1} from step 10. We update the velocity field $\tilde{U}^n$ to $\tilde{U}^{n+1,\star}$ by discretizing equation (37),

$$\tilde{U}^{n+1,\star} = \tilde{U}^n - \Delta t\Big\{\Big[\big(\tilde{U}^{\text{ADV},(2)} + w_0^{n+1/2}e_r\big)\cdot\nabla\big]\tilde{U}\Big\}^{n+1/2}$$

$$-\Delta t\big(\tilde{U}^{\text{ADV},(2)} \cdot e_r\big)\left(\frac{\partial w_0^{n+1/2}}{\partial r}\right)e_r$$

$$+\Delta t\left[-\frac{1}{\rho^{n+1/2}}G\pi^{n-1/2} + \frac{1}{\rho_0}G\pi_0^{(2)} - \frac{\big(\rho^{n+1/2} - \rho_0^{n+1/2}\big)}{\rho^{n+1/2}}ge_r\right], \quad (76)$$

where $\rho^{n+1/2} = (\rho^n + \rho^{n+1})/2$ and G approximates a cell-centered gradient from nodal data. The construction of $([(\tilde{U}^{\text{ADV},(2)} + w_0^{n+1/2}e_r)\cdot\nabla]\tilde{U})^{n+1/2}$ is described in Paper II, Appendix A, with $V = \tilde{U}^{\text{ADV},(2)} + w_0^{n+1/2}e_r$ and s set to each component of $\tilde{U}^n$ individually.

Finally, we impose the divergence constraint from equation (39),

$$\nabla \cdot \Big(\beta_0^{n+1/2}\tilde{U}^{n+1}\Big) = \beta_0^{n+1/2}\Big(S^{n+1} - \overline{S}^{n+1}\Big),$$

by defining $V = \tilde{U}^{n+1,\star} + (\Delta t/\rho^{n+1/2})G\pi^{n-1/2}$ and solving

$$L_\beta^\rho \phi = D\Big(\beta_0^{n+1/2}V\Big) - \beta_0^{n+1/2}\Big(S^{n+1} - \overline{S}^{n+1}\Big), \quad (77)$$

for nodal values of ϕ, where $\beta_0^{n+1/2} = (\beta_0^n + \beta_0^{n+1})/2$ and L_β^ρ is the standard bilinear finite element approximation to $\nabla \cdot (\beta_0^{n+1/2}/\rho^{n+1/2})\nabla$. In this step, D is a discrete second-order operator that approximates the divergence at nodes from cell-centered data and satisfies $\mathbf{G} = -D^T$. (See Almgren et al. [1996] for a detailed discussion of this approximate projection; see Almgren et al. [2000] for a discussion of this particular form of the projection operand.) We solve the linear system of equation (77) using multigrid V-cycles with Gauss-Seidel relaxation.

We determine the new time velocity field from

$$\tilde{\mathbf{U}}^{n+1} = \mathbf{V} - \frac{1}{\rho^{n+1/2}} \mathbf{G}\phi, \qquad (78)$$

and the new time-centered perturbational pressure from

$$\pi^{n+1/2} = \frac{1}{\Delta t} \phi.$$

STEP 12. *Compute a new Δt.* Compute Δt for the next time step with the procedure described in § 3.4, using w_0 as computed in step 6 and $\tilde{\mathbf{U}}^{n+1}$ as computed in step 11. We use this Δt in the next time step.

This completes the time advancement of the algorithm.

3.3. Initialization

We start each calculation with user-specified initial values for $\rho, X_k,$ and T, as well as an initial background state. In order for the low Mach number assumption to hold, the initial data must be thermodynamically consistent with the initial background state. In addition, the initial velocity field must satisfy an initial approximation to the divergence constraint. We use an iterative procedure to compute both an initial right-hand side for the constraint equation and an initial velocity field that satisfies the constraint. The user specifies the number of iterations, N_{iters}^S, in this first step of the initialization procedure.

The initial perturbational pressure also needs to be determined for use in steps 2, 7, and 11. This is done through a second iterative procedure which follows the time advancement algorithm as described in steps 1–11 in § 3.2. The user specifies the number of iterations, N_{iters}^π, in this second step of the initialization procedure. The details for both iterations are given below.

STEP 0. *Initialization.* Start with initial data $X_k^{\text{init}}, \rho^{\text{init}}, T^{\text{init}}$, an initial base state, and an initial guess for the velocity, $\mathbf{U}^{\text{init}}$. Use the equation of state to determine $(\rho h)^{\text{init}}$. Set $w_0^1 = 0$ as an initial approximation. Compute β_0^{init} as a function of the initial data. Then, project $\mathbf{U}^{\text{init}}$ using β_0^{init} and $S = \rho H_{\text{ext}}$, giving $\mathbf{U}^{0,1}$. The next part of the initialization process proceeds as follows.

a) Do $\nu = 1, \ldots, N_{\text{iters}}^S$.

   i) Estimate Δt^ν using $\mathbf{U}^{0,\nu}$ and w_0^ν.
   ii) React State$[\rho^{\text{init}}, (\rho h)^{\text{init}}, X_k^{\text{init}}, T^{\text{init}}, (\rho^{\text{init}} H_{\text{ext}})] \rightarrow [\rho^{\text{out}}, (\rho h)^{\text{out}}, X_k^{\text{out}}, T^{\text{out}}, (\rho\dot{\omega}_k)^{0,\nu}]$.
   iii) Compute $S^{0,\nu}$ from equation (19) using $(\rho\dot{\omega}_k)^{0,\nu}$ and the initial data.
   iv) Compute $\overline{S}^{0,\nu} = \text{Avg}(S^{0,\nu})$.
   v) Compute $w_0^{\nu+1}$ as in step 1c using $\overline{S}^{0,\nu}$ and $\psi^{n-1/2} = 0$.
   vi) Project $\mathbf{U}^{0,\nu}$ using β_0^{init} and $(S^{0,\nu} - \overline{S}^{0,\nu})$ as the source term. This yields $\mathbf{U}^{0,\nu+1}$.

End do.
   Define $S^0 = S^{0,N_{\text{iters}}^S}$, $w_0^{-1/2} = w_0^{N_{\text{iters}}^S + 1}$, $\Delta t^0 = \Delta t^{N_{\text{iters}}^S}$, and $\mathbf{U}^0 = \mathbf{U}^{0,N_{\text{iters}}^S + 1}$.

Next, we need to construct an approximation to the time-centered perturbational pressure, π, and an approximation to

the divergence constraint at the end of the first time step. As initial approximations, set $S^{1,0} = S^0$, $\eta_\rho^{-1/2} = 0$, $\psi^{-1/2} = 0$, and $\pi^{-1/2} = 0$.

b) Do $\nu = 0, \ldots, N_{\text{iters}}^\pi - 1$.

   i) Perform steps 1–11 as described above, using $S^{1/2,\star} = (S^0 + S^{1,\nu})/2$ in step 1 as described. The only other difference in the time advancement is that in step 11 we define $\mathbf{V} = (\tilde{\mathbf{U}}^{1,\star} - \tilde{\mathbf{U}}^0)$ and solve (the motivation for this form of the projection in the initial pressure iterations is discussed in Almgren et al. 2000)

$$L_\beta^\rho \phi = D\left(\beta_0^{1/2} \mathbf{V}\right) - \beta_0^{1/2}\left[\left(S^1 - \overline{S}^1\right) - \left(S^0 - \overline{S}^0\right)\right]. \quad (79)$$

We discard the new velocity resulting from this, but keep the new value for $\pi^{1/2} = \pi^{-1/2} + (1/\Delta t)\phi$. These steps also yield new scalar data at time Δt, which we discard, and new values for $\eta_\rho^{1/2}$ (step 8), $\psi^{1/2}$ (step 8), $S^{1,\nu+1}$ (step 10), and $\pi^{1/2}$ (step 11), which we keep.
   ii) Set $\pi^{-1/2} = \pi^{1/2}$, $\eta_\rho^{-1/2} = \eta_\rho^{1/2}$, and $\psi^{-1/2} = \psi^{1/2}$.

End do.
   Finally, we define $S^1 = S^{1,N_{\text{iters}}^\pi}$.

3.4. Computing the Time Step

There are several constraints on the time step. Effectively, we compute the time step based on each constraint separately, then take the minimum value of the various time steps computed.

The first set of constraints is based on the standard CFL condition for explicit methods. The user sets a CFL factor, σ^{CFL}, between 0 and 1. Because we advance the base state with w_0 only and the full state with $(\tilde{\mathbf{U}} + w_0 \mathbf{e}_r)$, we have two separate constraints based on the CFL condition. For a calculation in n_{dim} dimensions ($n_{\text{dim}} = 2$ or 3), the first constraint is

$$\Delta t_{\mathbf{U}} = \sigma^{\text{CFL}} \min_{i=1\ldots n_{\text{dim}}} \{\Delta t_i\}, \qquad (80)$$

where

$$\Delta t_i = \min_{\mathbf{x}} \left\{ \frac{\Delta x_i}{|\tilde{U}_i + w_0^{\text{cell}} \mathbf{e}_r \cdot \mathbf{n}_i|} \right\}. \qquad (81)$$

Here w_0^{cell} is the value of w_0 averaged from the cell edges to each cell center, $\mathbf{n}_i$ is the normal in the ith coordinate direction, and $\min_{\mathbf{x}}$ is the minimum taken over all computational grid cells in the domain.

The second constraint is based entirely on w_0,

$$\Delta t_{w_0} = \sigma^{\text{CFL}} \min_j \left\{ \frac{\Delta r}{|w_{0j}|} \right\}, \qquad (82)$$

where Δr is the spacing of the radial arrays such as the base state and w_{0j} is the value of w_0 at a radius of $j\Delta r$. For plane-parallel simulations $\Delta r = \Delta x$, but in the spherical simulations Δr and Δx need not be the same.

An additional constraint is based on the forcing terms rather than the velocities. This constraint is necessary when a calculation is started from rest, since in that case the velocity-based time step would be infinite.

Here, we define

$$\Delta t_F = \min_{i=1\ldots n_{\text{dim}}} \{\Delta t_{F_i}\}, \qquad (83)$$

where

$$\Delta t_{F_i} = \sqrt{2\Delta x_i / F_{i\max}}, \qquad (84)$$

where $F_{i\,\mathrm{max}}$ is the maximum buoyancy force in the ith coordinate direction.

A final time step constraint is needed to prevent local expansion from numerically emptying a cell. We require that the density be reduced by no more than 40% in a single time step; this is expressed in terms of constraining the time step so that $\Delta t \leq \Delta t_S$, where Δt_S is defined at the beginning of each time step so that

$$\Delta t_S (\nabla \cdot \tilde{\boldsymbol{U}}^n) \leq 0.40, \qquad (85)$$

in every cell.

For the initial iterations described in § 3.3 above, none of these methods may give a reasonable time step if there is no initial velocity field. In that case, we set the time step to the fully compressible time step constraint—i.e., that determined by the bulk velocity plus the sound speed.

4. NUMERICAL RESULTS

In this section we present results exploring different features of the low Mach number algorithm in a plane-parallel geometry. The first set of simulations are bubble rise problems with reactions. We compare the low Mach number results with compressible results and also perform a convergence study of the low Mach number method. The second set of simulations are of long-timescale convection; again we compare with compressible results and, in addition, examine the long-time behavior of the thermodynamic pressure relative to the background pressure to verify that the model assumptions continue to hold. All of these tests are performed with the general astrophysical equation of state (Timmes & Swesty 2000), suitable to the conditions in a white dwarf.

4.1. Background State

For each of our numerical tests we define the background state in three parts, as in Paper II. The central portion of the domain is initialized with a one-dimensional hydrostatic white dwarf model. The model is created by specifying a base density of 2.6×10^9 g cm^{-3} and base temperature of 7×10^8 K and integrating the equation of hydrostatic equilibrium outward while constraining the model to be isentropic. The composition is held constant at 0.3 ^{12}C and 0.7 ^{16}O, and the gravitational acceleration is fixed at -1.5×10^{10} cm s^{-2}. This procedure provides a reasonable approximation of the state of the white dwarf just before runaway.

Below this layer, we decrease the entropy by a factor of 3 and create a convectively stable layer by integrating downward with a constant entropy gradient, so that the entropy decreases slowly toward the bottom of the domain. This layer acts as part of the lower boundary condition to insulate the dynamics in the unstable layer from the effects of the lower boundary of the computational domain. The entropy drop here is large enough that the temperatures in this layer are $<10^7$ K, and the thermonuclear reactions are effectively turned off.

The upper portion of the domain represents the region beyond the outer boundary of the white dwarf, and different approximations are used there for the compressible and low Mach number models. For each model we define a "density cutoff." Once the density drops below this value, the integration is stopped and the material above it is held at constant density and temperature. In the compressible case the pressure is evaluated from the density and temperature; in the low Mach number model the base state pressure is held constant.

For the compressible calculations, the density cutoff is set to 10^{-4} g cm^{-3}. We also impose that the temperature is never allowed to drop below 10^7 K. Figure 1 of Paper II shows the initial temperature, density, entropy, and adiabatic indices [Γ_1 and $\gamma_e \equiv p/(\rho e) + 1$] as a function of height for the compressible background.

For the low Mach number model, we also impose an "anelastic cutoff"; this is the value of density below which we define β_0 by keeping β_0/ρ_0 constant and is used in order to suppress spurious wave formation at the outer boundary of the star. In the calculations shown here, both the density cutoff and the anelastic cutoff are set to 3×10^6 g cm^{-3}.

4.2. Reacting Bubble Rise

To test the coupling of reactions to the hydrodynamics, we consider a plane-parallel carbon/oxygen white dwarf model seeded with temperature perturbations. For these calculations we restrict ourselves to a plane-parallel geometry in order to more easily facilitate the comparisons to a fully compressible code.

We use a single-step ^{12}C(^{12}C, γ) ^{24}Mg reaction. The carbon mass fraction equation appears as

$$\frac{DX(^{12}\mathrm{C})}{Dt} = -\frac{1}{12} \rho X(^{12}\mathrm{C})^2 f_{\mathrm{Coul}}[N_A \langle \sigma v \rangle], \qquad (86)$$

where $N_A \langle \sigma v \rangle$ is evaluated using the reaction rate from Caughlan & Fowler (1988). The Coulomb screening factor, f_{Coul}, is evaluated using the general routine from the Kepler stellar evolution code (Weaver et al. 1978), which implements the work of Graboske et al. (1973) for weak screening and the work of Alastuey & Jancovici (1978) and Itoh et al. (1979) for strong screening. Larger networks can easily be accommodated.

The initial conditions for the bubble rise problem are defined to be the background state, as defined in § 4.1, perturbed by the addition of local temperature variations (with corresponding density perturbations that keep the perturbed regions in pressure equilibrium with the background) of the form

$$T_{i,j} = (T_{\mathrm{init}})_j \left\{ 1 + \sum_{m=1}^3 a_m \left[1 + \tanh \left(2 - \frac{d_m}{\sigma_m} \right) \right] \right\},$$
$$\rho_{i,j} = \rho \left(p_{0j}, T_{i,j}, (X_{k,\mathrm{init}})_j \right). \qquad (87)$$

Here, i and j are the lateral and vertical zone indices, respectively, T_{init} is the initial background temperature, p_0 is the base state pressure, and $X_{k,\mathrm{init}}$ is the initial mass fraction of species k. The distance d_m is simply found as $d_m^2 = (x_i - x_m)^2 + (r_j - r_m)^2$. No explicit heating source term is included—these perturbations are large enough to begin localized carbon burning in the model star. In addition to the burning in the rising bubbles, the conditions at the base of our convectively unstable layer (where $\rho = 2 \times 10^9$ g cm^{-3} and $T = 7 \times 10^8$ K), which correspond to those at the center of a white dwarf a short time before a SN Ia, are such that low-level reactions also occur here.

4.2.1. Comparison with Compressible

This first test is similar to that presented in Paper II, except now the heating is provided by reactions. For this test we use three perturbations, whose coordinates x_m and r_m, width σ_m, and amplitude a_m are listed in Table 1. We compare the low Mach number results with both an unsplit and dimensionally split implementation of the compressible upwind method of Colella (1990).

The domain is 2.16×10^8 cm by 3.6×10^8 cm, of which the bottom 0.5×10^8 cm is the low-entropy layer. The resolution is 384×640 cells. Periodic boundary conditions are used on the

ALMGREN ET AL.

TABLE 1
PARAMETERS FOR INITIAL TEMPERATURE PERTURBATIONS

m	a_m	x_m (cm)	r_m (cm)	σ_m (cm)
1..........................	0.15	5.0×10^7	6.5×10^7	2.5×10^6
2..........................	0.30	1.2×10^8	8.5×10^7	2.5×10^6
3..........................	0.225	2.0×10^8	7.5×10^7	2.5×10^6

NOTE.—See eq. (87).

left and right domain edges. The low Mach number runs use a solid wall boundary at the lower boundary and outflow at the upper boundary. The fully compressible simulations use a hydrostatic lower boundary (with the velocity given a zero gradient) and a zero-gradient upper boundary (with the velocity restricted from inflowing, i.e., it is set to 0 if it is negative). The compressible boundaries are described in more detail in Zingale et al. (2002).

Figure 1 shows the temperature (calculated from the equation of state given enthalpy, density, and composition) and ^{24}Mg abundance after 2.5 s of evolution, for the split and unsplit compressible algorithms and the low Mach number algorithm. Generally, the results agree well between the algorithms. As discussed in Papers I and II, the bubbles in the low Mach number case are slightly narrower than those from the compressible runs, but as we showed there, the magnitude of the disparity is comparable to that between different compressible algorithms. We note that the dimensionally split compressible algorithm used in this paper is different from the split algorithm used in Papers I and II. With this new algorithm, we do not see the temperature oscillations that we attributed to dimensional splitting in Paper I.
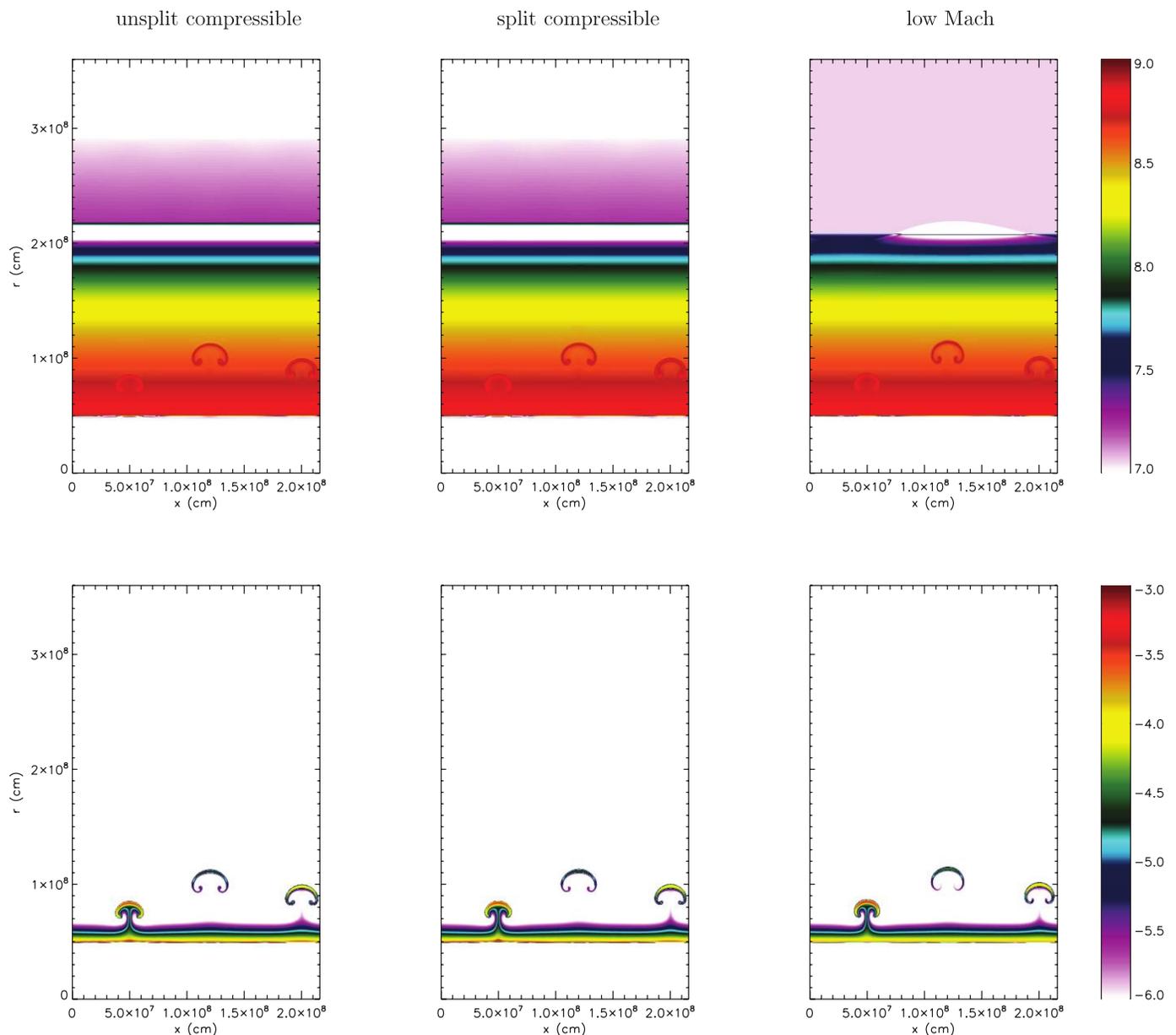
FIG. 1.—Comparison of the low Mach number (*left*) and compressible (*right*) solutions for the three-bubble test. Shown are the log of temperature (*top row*) and ^{24}Mg mass fraction (*bottom row*) at $t = 2.5$ s.

Another feature of the algorithm that we explore with this simulation is the effect of replacing Γ_1 by $\overline{\Gamma}_1$ in the definition of α (see eq. [10]). We consider equation (9) in the form

$$\nabla \cdot \boldsymbol{U} + \frac{1}{\Gamma_1 p_0} \frac{Dp_0}{Dt} = S.$$

We argued in Paper I that we could replace Γ_1 in the above equation by $\overline{\Gamma}_1$, allowing us to write equation (9) in the form of equation (12). Instead, we could substitute a more general expression, $\Gamma_1 = \overline{\Gamma}_1 + \delta\Gamma_1$, into equation (9), giving

$$\nabla \cdot \boldsymbol{U} + \frac{1}{(\overline{\Gamma}_1 + \delta\Gamma_1)p_0} \boldsymbol{U} \cdot \nabla p_0 = S - \frac{1}{(\overline{\Gamma}_1 + \delta\Gamma_1)p_0} \frac{\partial p_0}{\partial t}.$$

Assuming that $\delta\Gamma_1 \ll \overline{\Gamma}_1$, we then have

$$\nabla \cdot \boldsymbol{U} + \frac{1}{\overline{\Gamma}_1 p_0} \boldsymbol{U} \cdot \nabla p_0$$
$$= S - \frac{1}{\overline{\Gamma}_1 p_0} \frac{\partial p_0}{\partial t} + \frac{\delta\Gamma_1}{\overline{\Gamma}_1^2 p_0} \frac{\partial p_0}{\partial t} + \frac{\delta\Gamma_1}{\overline{\Gamma}_1^2 p_0} \boldsymbol{U} \cdot \nabla p_0, \quad (88)$$

The base state evolution equation is the average of this over a layer,

$$\nabla \cdot w_0 \boldsymbol{e}_r + \frac{1}{\overline{\Gamma}_1 p_0} w_0 \boldsymbol{e}_r \cdot \nabla p_0$$
$$= \overline{S} - \frac{1}{\overline{\Gamma}_1 p_0} \frac{\partial p_0}{\partial t} + \overline{\left(\frac{\delta\Gamma_1}{\overline{\Gamma}_1^2 p_0} \tilde{\boldsymbol{U}} \cdot \nabla p_0 \right)}.$$

Subtracting this from equation (88), we have

$$\nabla \cdot \tilde{\boldsymbol{U}} + \frac{1}{\overline{\Gamma}_1 p_0} \tilde{\boldsymbol{U}} \cdot \nabla p_0$$
$$= S - \overline{S} + \frac{\delta\Gamma_1}{\overline{\Gamma}_1^2 p_0} (\psi + \tilde{\boldsymbol{U}} \cdot \nabla p_0) - \overline{\left(\frac{\delta\Gamma_1}{\overline{\Gamma}_1^2 p_0} \tilde{\boldsymbol{U}} \cdot \nabla p_0 \right)}.$$

These can be written more compactly as

$$\frac{\partial w_0}{\partial r} = \overline{S} - \frac{1}{\overline{\Gamma}_1 p_0} \psi + \overline{\left(\frac{\delta\Gamma_1}{\overline{\Gamma}_1^2 p_0} \tilde{\boldsymbol{U}} \cdot \nabla p_0 \right)}, \quad (89)$$

for plane-parallel geometries (analogous to eq. [35]), and

$$\nabla \cdot (\beta_0 \tilde{\boldsymbol{U}}) = \beta_0 \left[S - \overline{S} + \frac{\delta\Gamma_1}{\overline{\Gamma}_1^2 p_0} \psi \right.$$
$$\left. + \frac{\delta\Gamma_1}{\overline{\Gamma}_1^2 p_0} \tilde{\boldsymbol{U}} \cdot \nabla p_0 - \overline{\left(\frac{\delta\Gamma_1}{\overline{\Gamma}_1^2 p_0} \tilde{\boldsymbol{U}} \cdot \nabla p_0 \right)} \right], \quad (90)$$

instead of equation (39). In order to solve this equation using the projection methodology, we consider a time-lagged approximation to the $\tilde{\boldsymbol{U}} \cdot \nabla p_0$ terms appearing on the right-hand side. We explore the effect of substituting equation (90) for equation (39) in both the final MAC projection (step 7) and the final projection (step 11) and the effect of using equation (89) in step 6.

Figure 2 shows a superposition of contours of the temperature from the original simulation (using just $\overline{\Gamma}_1$ in eq. [9]) and the temperature from the same simulation except using the $\delta\Gamma_1$ correction
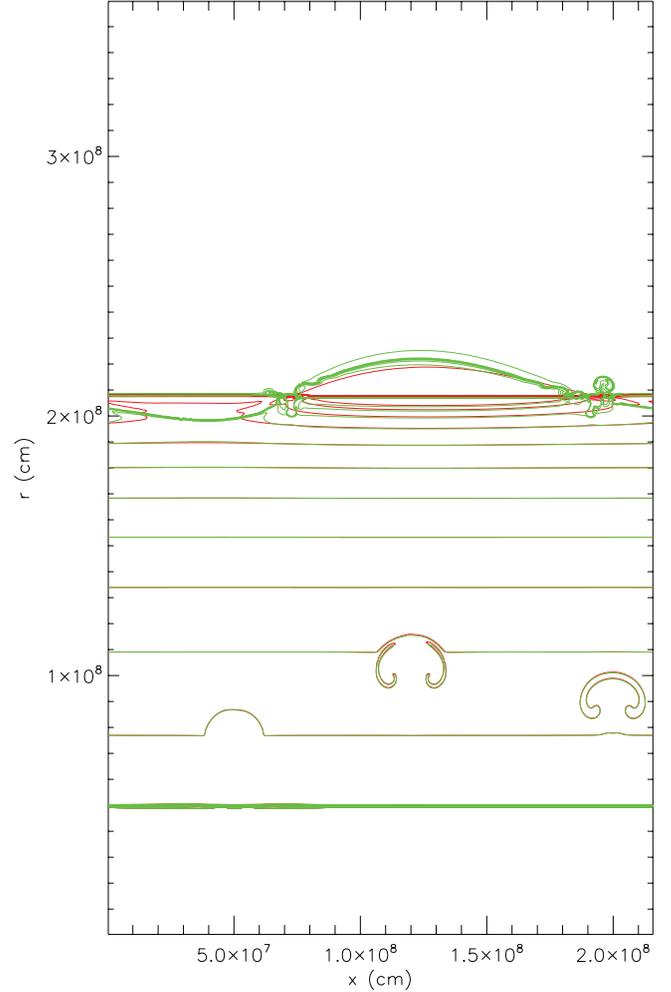
Fig. 2.—Comparison of the effect of using only $\overline{\Gamma}_1$ (*red*) vs. the lagged $\delta\overline{\Gamma}_1$ correction (*green*). Here, the temperature is plotted, with 12 contours equally spaced in log T in the range 10^7 K $\leq T \leq 8 \times 10^8$ K. We see excellent agreement between the simulations, demonstrating that it is reasonable to use only $\overline{\Gamma}_1$ in eq. (10).

in the projections. We see that there is very little difference in the two temperature fields in the region surrounding the bubbles, supporting our original substitution of $\overline{\Gamma}_1$ for Γ_1 in the velocity constraint equation. The region at the top of the atmosphere in the calculation with the $\delta\Gamma_1$ terms develops some vortices—this is likely an interaction between these additional terms and the steep falloff at the top of the initial model. Since this is far from the region of interest (the bubbles) and since these correction terms are not part of the regular algorithm, we did not explore this vortex generation in detail. In future calculations, we will continue to monitor $\delta\Gamma_1$ to further assess whether additional corrections are needed.

4.2.2. *Convergence Study*

In the calculations considered here we zoom in on a single reacting bubble, corresponding to $m = 2$ in Table 1. The domain spans 1.44×10^8 cm in the horizontal and vertical directions, of which the bottom 0.1×10^8 cm is the low-entropy layer. We center the hot spot laterally in the domain. The calculations are run with a fixed time step to $t = 1.0$ s, and data is presented at intervals of 0.2 s. The time steps for the coarse, medium, and fine resolutions are $\Delta t = 0.02, 0.01$, and 0.005 s, respectively. The resolutions are $\Delta r = 1.125 \times 10^6, 5.625 \times 10^5$, and 2.8125×10^5 cm,
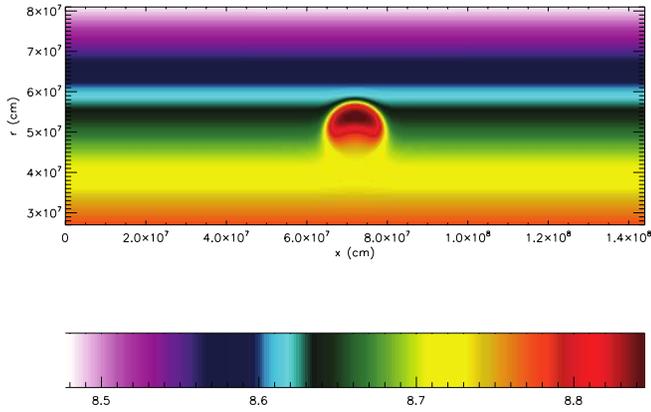
respectively. The boundary conditions are solid wall on the lower boundary, periodic on the lateral boundaries, and outflow at the upper boundary.

To compute rates of convergence, we first compute the errors between data differing by a factor of 2 in resolution. The error is defined at the coarser of the two resolutions by the difference between the coarser calculation and the volumetrically averaged finer calculation of each set. The L_1 norm of each error is then computed, and the ratio of the coarse–medium error to the medium–fine error is computed and presented in the table. Ratios of approximately 4 denote second-order convergence.

For these simulations, the sharpness of the transition at the artificial low-entropy layer at the bottom of the domain introduces errors at the interface that obscure the convergence behavior of the scheme. In addition, we want to focus on the bubble dynamics rather than the upper atmosphere where the flow is smoother. For these reasons, we measure errors in a subset of the domain, from 0.27×10^8 cm to 0.81×10^8 cm in the vertical direction. Figure 3 shows the temperature field at $t = 1$ s in the region of interest.

In Table 2 we present the ratios of the L_1 norms of the errors in velocity, perturbational density, enthalpy, and ^{24}Mg abundance. At early times, the data shows second-order behavior for all of the primary variables and a reduced rate for the enthalpy, which is caused by the interaction of the interpolated initial data with the equation of state. At intermediate times, we begin to see a reduced convergence rate $\approx h^{1.5}$ in the ^{24}Mg abundance and perturbational density. We believe that this reduced rate results from the extreme sensitivity of the reaction rate to temperature, $O(T^{23})$ (Woosley et al. 2004).

Another important test of the behavior of the methodology is the degree to which the solution drifts from the equation of state, i.e., the degree to which the thermodynamic pressure, defined by the equation of state as a function of density, enthalpy, and composition, differs from p_0 over time. This drift occurs because the algorithm enforces the Lagrangian derivative of the equation of

state through the divergence constraint on velocity, but does not strictly enforce the equation of state itself at each time step. Consequently, although $p(\rho, h, X_k) \equiv p_0$ at initial time, this equality is not strictly maintained over time.

In this calculation, in addition to measuring the difference between coarse and fine solutions, we monitor two quantities that reflect this drift. The first is $(\delta p)_{\text{drift}} = |p(\rho, h, X_k) - p_0|$, and the second is $(\delta T)_{\text{drift}} = |T_p - T_h|$, where T_p is defined from the equation of state using ρ, p_0, and X_k, and T_h is defined from ρ, h, and X_k.

In Table 3 we present the convergence rates of $(\delta p)_{\text{drift}}/p_0$ and $(\delta T)_{\text{drift}}$. We note that the magnitude of $(\delta p)_{\text{drift}}$ never exceeds 0.01% of p_0 at any point in the region of interest. Furthermore, the magnitude of $(\delta T)_{\text{drift}}$ never exceeds 1% of T_h. In addition, we see from Table 3 that both of these quantities show strict second-order convergence. We note that no values are shown for $t = 0.0$ in Table 3 because $(\delta p)_{\text{drift}}$ and $(\delta T)_{\text{drift}}$ are identically zero there at all resolutions.

4.3. Plane-Parallel Convection

In this section we consider longer time convection in our model atmosphere, again in a plane-parallel geometry for the purpose of easier comparison between the compressible and low Mach number algorithms. In order to allow for better control over the heating that drives the convection, we use a prescribed heating rate, specified through H_{ext} as defined in the above algorithm.

For the tests presented in this section, we use a heating term of the form

$$H_{\text{ext}i,j} = H_0 \exp\left[\frac{-(r_j - r_{\text{layer}})^2}{W^2}\right]$$
$$\times \left[1 + \sum_{m=1}^{n_{\text{pert}}} b_m \sin\left(\frac{k_m \pi x_i}{L_x} + \Psi_m\right)\right]. \quad (91)$$

Here, H_0 is the absolute heating rate (to be specified below), r_{layer} is the height at which the heating is centered, and L_x is the width of the domain. The amplitudes, b_m, modes, k_m, and phases, Ψ_m, of the sinusoidal perturbations are listed in Table 4.

4.3.1. Sponge Layer

The large drop in density at the surface of the star results in high velocities in the region above the surface when high heating rates

TABLE 3
RATIOS OF L_1 ERRORS OF $(\delta p)_{\text{drift}}/p_0$ AND $(\delta T)_{\text{drift}}$

t	$(\delta p)_{\text{drift}}/p_0$	$(\delta T)_{\text{drift}}$
0.2..............................	3.8	3.5
0.4..............................	4.2	4.0
0.6..............................	4.2	3.9
0.8..............................	4.2	4.0
1.0..............................	4.0	3.9

TABLE 2
RATIOS OF L_1 ERRORS OF DYNAMIC AND THERMODYNAMIC VARIABLES

t	u	v	$\rho - \rho_0$	h	$X(^{24}\text{Mg})$
0.0...................	4.2	4.0	4.0	3.5	...
0.2...................	3.8	4.0	3.8	3.2	4.1
0.4...................	3.7	3.9	3.9	3.7	3.3
0.6...................	3.8	3.9	3.9	3.8	3.6
0.8...................	3.8	4.2	3.5	3.8	2.8
1.0...................	4.1	4.0	2.8	3.6	2.9

TABLE 4
PARAMETERS FOR HEATING RATES

m	b_m	k_m	Ψ_m
1................................	0.00625	2	0
2................................	0.01875	6	$\pi/3$
3................................	0.01250	8	$\pi/5$
4................................	0.00250	1	0.562

NOTE.—See eq. (91).

are used in a plane-parallel geometry. This region should not affect the dynamics below the surface in the convecting regions of the star. However, because the time step in the low Mach number code is limited by the highest velocity in the computational domain, the efficiency gains of the low Mach number algorithm are reduced if those velocities persist.

To address this we employ a damping technique commonly used in modeling atmospheric convection (see, e.g., Durran 1990). A forcing term is added to the velocity update before the final projection at the end of each time step in the form

$$\boldsymbol{U}^{\mathrm{new}} = \boldsymbol{U}^{\mathrm{old}} - \Delta t \kappa f_{\mathrm{damp}} \boldsymbol{U}^{\mathrm{new}}.$$

We note that solving this implicitly for $\boldsymbol{U}^{\mathrm{new}}$ is equivalent to multiplying $\boldsymbol{U}^{\mathrm{old}}$ by the factor $1/(1 + \Delta t \kappa f_{\mathrm{damp}})$ to define $\boldsymbol{U}^{\mathrm{new}}$.

The sponge profile, f_{damp}, takes the form

$$f_{\mathrm{damp}} = \begin{cases} 0, & z < z_{\mathrm{sp}}, \\ \frac{1}{2}\left\{1 - \cos\left[\pi\left(\frac{z - z_{\mathrm{sp}}}{z_{\mathrm{tp}} - z_{\mathrm{sp}}}\right)\right]\right\}, & z_{\mathrm{sp}} \le z < z_{\mathrm{tp}}, \quad (92) \\ 1, & z \ge z_{\mathrm{tp}}. \end{cases}$$

Here, z_{sp} is the height above which the damping term becomes nonzero, and z_{tp} is the height at which the forcing reaches its maximum. We can think of $1/\kappa$ as the timescale over which we want to drive the velocities back to zero. Since the background profiles are allowed to shift, we define the location of the sponge dynamically in terms of the background density.

For the low Mach number algorithm we simply multiply $\tilde{\boldsymbol{U}}^{n+1,\star}$ in step 11 by the factor above before solving the elliptic equation to impose the divergence constraint. In the compressible algorithm, the velocity is multiplied by this factor at the end of each time step. In § 4.3.2 we explore the effect of the damping by contrasting compressible calculations with and without the sponge layer as well as the low Mach number calculation with a sponge layer.

4.3.2. Convection Example: Comparison with Compressible

The first convection problem we consider is run with 320×512 cells in a domain of 2.5×10^8 cm by 4.0×10^8 cm, of which the bottom 10^8 cm is the low-entropy layer. We note that this layer is thicker than that used in the bubble rise simulations, because we wish to further insulate the convection from the effects of the lower boundary. For the sponge layer $\kappa = 100$ s^{-1}. The average time step in the low Mach number calculations is $\overline{\Delta t} \sim 10^{-3}$ s, so our choice of κ means that the velocities in the sponge layer will be damped over $(1/\kappa)/\overline{\Delta t} \sim 10$ time steps. In order to compare our low Mach number results with those from the compressible algorithm, for these simulations we fix the sponge transition heights at $z_{\mathrm{sp}} = 2.19140625 \times 10^8$ cm and $z_{\mathrm{tp}} = 2.97265625 \times 10^8$ cm. As with the bubble rise calculations, the lateral boundary conditions are periodic. In the compressible simulations, the upper boundary is again zero gradient (with the velocity prevented from inflowing) and the lower boundary is hydrostatic (with the velocity given a zero gradient), while in the low Mach number simulation the lower boundary is solid wall while the upper boundary is outflow.

For the heating we choose $r_{\mathrm{layer}} = 1.25 \times 10^8$ cm (i.e., just 250 km above the base of our convectively unstable layer) and $W = 10^7$ cm. For this example, we include only the first three perturbational modes ($n_{\mathrm{pert}} = 3$) from Table 4. We want to choose H_0 large enough that the compressible algorithm can be used for

comparison, but not so large that we exceed the limits of validity of the low Mach number approach. We find that $H_0 = 2.5 \times 10^{16}$ erg g^{-1} s^{-1} results in a Mach number that remains below 0.4 in the atmosphere. For reference, the thermonuclear energy generation rate at the base of the convectively unstable layer (away from the perturbations) in the previous test was $\sim 3 \times 10^{13}$ erg g^{-1} s^{-1}, very close to the analytic estimate provided by Woosley et al. (2004) for our base conditions ($\rho = 2 \times 10^9$ g cm^{-3} and $T = 7 \times 10^8$ K). Since our choice of H_0 is much higher than the energy generation rate we would expect during the smoldering phase of SNe Ia evolution, we expect this to be a very demanding test of the low Mach number algorithm.

Figure 4 shows the temperature field after 5 s and after 10 s for the low Mach number algorithm and for the compressible algorithm with and without the sponge layer. We consider a region of interest, which we define as 10^8 cm $\le r \le 2.2 \times 10^8$ cm—i.e., the domain excluding the low-entropy region at the bottom and sponge layer at the top. In the region of interest we see good qualitative agreement in the overall features of the solution in all three cases; however, because of the highly unstable character of convection over long times we do not expect point-by-point agreement. A more appropriate comparison is to examine the overall statistics of the convective flow. Here, since we are not including reactions we focus on the average and rms fluctuations of temperature. In particular, we define the lateral average of T,

$$\langle T \rangle_j = \frac{1}{N_x} \sum_{i=1}^{N_x} T_{i,j}, \quad (93)$$

where N_x is the number of cells in the lateral direction, and the rms fluctuations,

$$(\delta T)_j = \left[\frac{1}{N_x} \sum_{i=1}^{N_x} \left(T_{i,j} - \langle T \rangle_j\right)^2\right]^{1/2}. \quad (94)$$

Figure 5 shows both the average and deviation of the temperature at both times. First, we examine the difference between the compressible solution with and without the sponge layer. At both 5 and 10 s, we see very strong agreement between these two runs in the region of interest. While the solutions differ both above and below the region of interest, this result gives us confidence in the location and strength of the sponge layer.

Next we compare the compressible and low Mach number solutions. Again, the solutions agree very well in the region of interest. In the low-entropy layer below the region of interest, we do see noticeable differences between the solutions; however, these deviations are small in magnitude and do not appear to affect the solution in the region of interest. (We attribute the low Mach number results to the small vortices penetrating the low-entropy layer from above, as seen in Fig. 4. We suspect the presence of these vortices is due to the reflecting wall boundary condition at the lower boundary.) For this calculation, we note that the magnitude of $(\delta p)_{\mathrm{drift}}/p_0$ never exceeds approximately 1% in the convectively unstable region below the sponge layer.

4.3.3. Convection Example: Long-Time Study

In our final simulation, we reduce the magnitude of the heating and simulate for a longer time. The domain for this simulation is 5×10^8 cm by 3.5×10^8 cm, of which the bottom 0.5×10^8 cm is the low-entropy layer. We use 640×448 cells and follow the large-scale convection to $t = 60$ s, with a time step set using a CFL number of 0.9. The location of the sponge is adjusted

compressible   compressible + sponge   low Mach
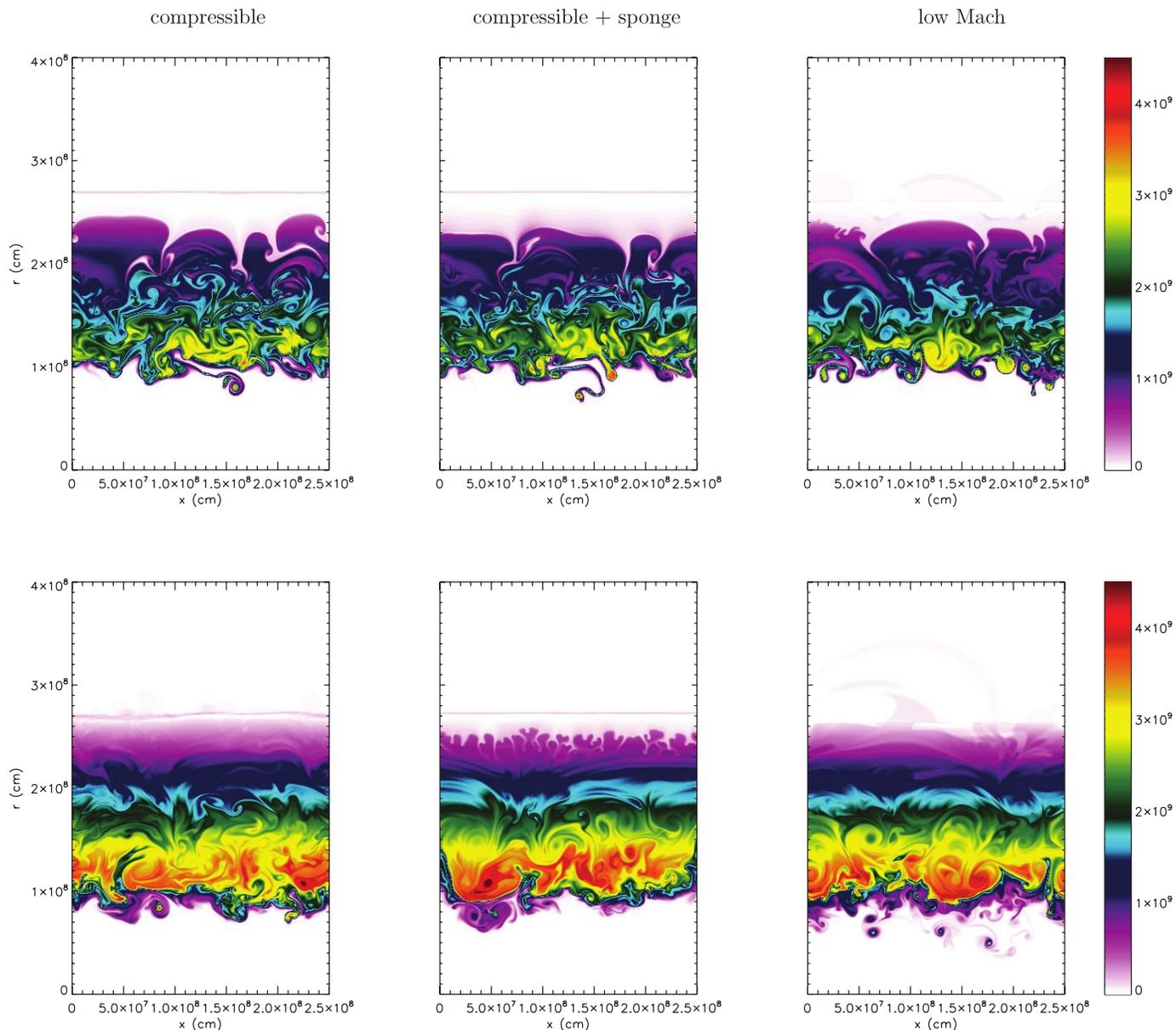
Fig. 4.—Temperature at $t = 5$ and 10 s in the first convection example. Shown are results using the compressible algorithm with and without a sponge layer and the low Mach number algorithm with a sponge layer.

dynamically as discussed in § 4.3.1, and we set $\kappa = 100$ s^{-1}. In particular, we define the middle of the transition region, $z_{md} = \frac{1}{2}(z_{tp} + z_{sp})$, to be the location of the density cutoff, i.e., where ρ_0 reaches 3.0×10^6 g cm^{-3}. We define z_{hw} as the location where $\rho_0 = 10^7$ g cm^{-3}. Then $z_{sp} = z_{md} - 2(z_{md} - z_{hw})$, and $z_{tp} = z_{md} + 2(z_{md} - z_{hw})$. The heating is again in the form of equation (91) with $r_{layer} = 7.5 \times 10^7$ cm, $W = 10^7$ cm, and $H_0 = 1.0 \times 10^{14}$. Here we use four perturbational modes ($n_{pert} = 4$), with the amplitudes, b_m, modes, k_m, and phases, Ψ_m, of the sinusoidal perturbations given in Table 4.

Figure 6 shows a time sequence of temperature and vorticity from this calculation in the lower 2.5×10^8 cm of the domain. In this example, the early-time dynamics shows the emergence of large-scale regular structures in the principal region of interest with some small-scale mixing at the boundary of the low-entropy region. At $t = 20$ s we begin to see the breakdown into smaller structures. At later times the temperature shows a large-scale lay-

ered structure with small-scale perturbations, while the vorticity shows that the flow is now dominated by small-scale mixing. For this simulation, the sponge effectively suppresses unphysical high velocities above the anelastic cutoff. Examination of the Mach number shows that the Mach number remains below 0.3 for the entire simulation, so that at this reduced heating the flow remains in the low Mach number regime.

Figure 7 shows the magnitude of $(\delta p)_{drift}/p_0$. For this calculation, we also note that this never exceeds approximately 1% in the convectively unstable region below the sponge layer, in spite of the long-time integration.

4.4. Large-Scale Convective Overturning

A new feature of the algorithm is the presence of η_ρ. This term serves to keep ρ_0 equal to the average density in a layer and keep p_0 equal to the hydrostatic pressure as determined by the average density.
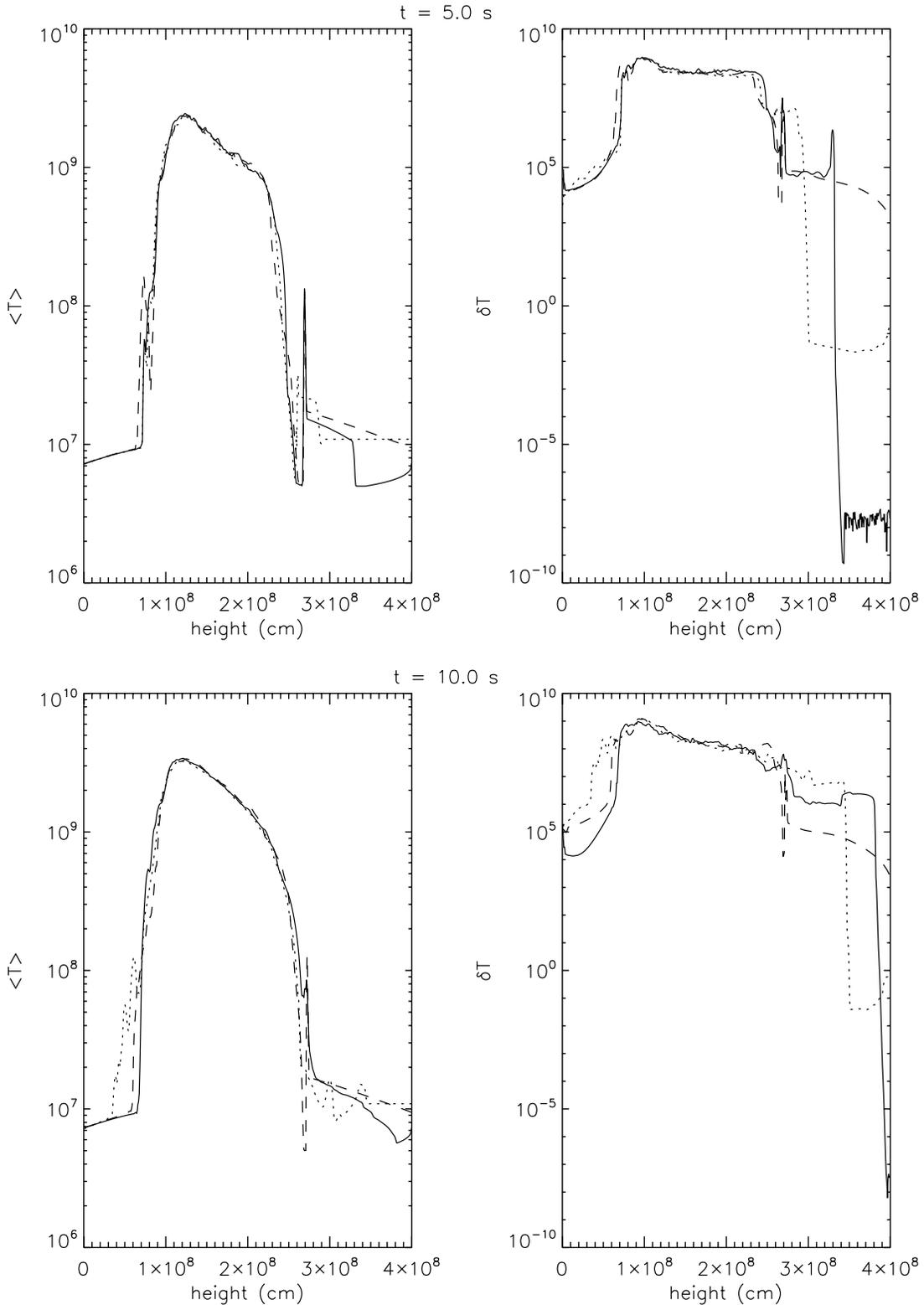
FIG. 5.—Comparison of the average temperature as a function of height, $\langle T \rangle$, and the deviation of temperature from the average, δT, for the compressible (*solid curves*), compressible with sponge (*dashed curves*), and low Mach number with sponge (*dotted curves*) calculations. Our region of interest is 10^8 cm $\leq r \leq 2.2 \times 10^8$ cm.

In typical problems of interest the evolution of the base state is very gradual relative to other motions, making it hard to see the effects of the η_ρ term. Here we present an example specifically designed to generate large-scale overturning of the density profile. This problem has no net heating; therefore, using the algorithm as presented in Paper II there would be no change in the base state. However, in this example the average density changes dramatically, and it is clear that the base state should reflect the change in average profiles.

The computational domain for this example is a box 0.3×10^8 cm wide and 1.2×10^8 cm high, from $z = 1.6 \times 10^8$ to 2.8×10^8 cm. We define the profile for density as $f(z_{\mathrm{model}})$ for

temperature   vorticity
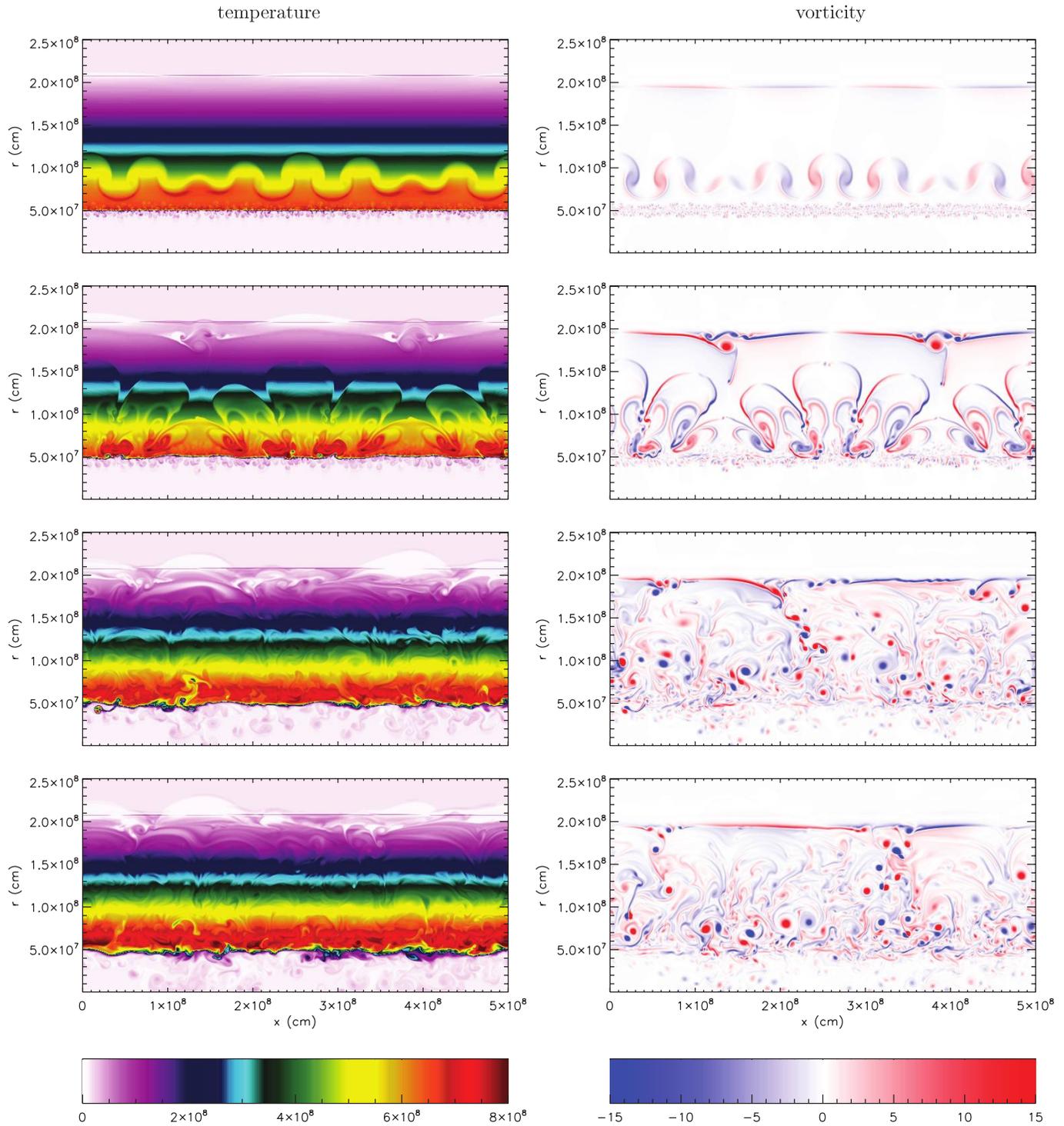
Fig. 6.—Temperature and vorticity evolution for the low heating rate, long-time evolution calculation, shown (from top to bottom) at 15, 20, 40, and 60 s. Note that the true range in vorticity for this simulation is -153 s^{-1} to 152 s^{-1}—the scale in the plot is reduced to show detail.

$z_{\mathrm{model}} = 1.6 \times 10^8$–$2.5 \times 10^8$ cm using interpolation of the model described in § 4.1. Then the base state density is defined by

$$\rho_0(z) =$$

$$\begin{cases} f(z), & 1.6 \times 10^8 \text{ cm} \leq z < 1.75 \times 10^8 \text{ cm}, \\ f(3.5 \times 10^8 \text{ cm} - z), & 1.75 \times 10^8 \text{ cm} \leq z < 1.9 \times 10^8 \text{ cm}, \\ f(z - 0.3 \times 10^8 \text{ cm}), & 1.9 \times 10^8 \text{ cm} \leq z \leq 2.8 \times 10^8 \text{ cm}. \end{cases}$$

We note that this density profile is no longer monotonic with height. The base state pressure is defined by setting the pressure at the top of the domain to the model pressure at $z_{\mathrm{model}} = 2.5 \times 10^8$ cm, then integrating hydrostatically downward in the domain. As in the previous examples, the composition is held constant at 0.3 ^{12}C and 0.7 ^{16}O.

We set the initial data to be identical to the base state at $t = 0$. The gravitational acceleration is fixed at -1.5×10^{10} cm s^{-2}. The initial density profiles are included in Figure 8.
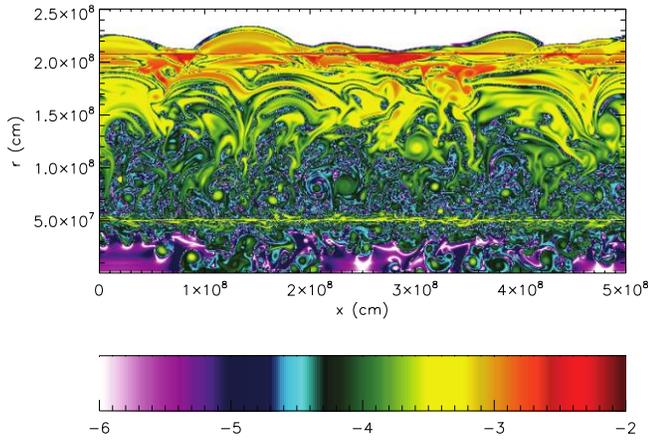
FIG. 7.—Plot of $\log\left[|(\delta p)_{\mathrm{drift}}|/p_0\right]$ at $t = 60$ s.

In order to trigger the convective overturning, for 1.75×10^8 cm $< z < 1.9 \times 10^8$ cm we set the initial velocity field to a large-scale rotational flow defined by

$$\tilde{U}(z) = \left[-200 \sin\left(4\pi z_s\right) \cos\left(4\pi z_s\right) \sin^2(\pi x_s),\right.$$
$$\left.200 \sin\left(\pi x_s\right) \cos\left(\pi x_s\right) \sin^2(4\pi z_s)\right],$$

where $x_s = x/(0.3 \times 10^8$ cm$)$ and $z_s = (z - 1.75 \times 10^8$ cm$)/(1.2 \times 10^8$ cm$)$; in the rest of the domain the initial velocity is set to zero. The initial projection then modifies this field to enforce the divergence constraint.

We present results at $t = 0$ and 0.85 s from two different calculations, both run with 128×512 cells. We note that at $t = 0.85$ s the maximum Mach number is approximately 0.24 in both calculations, so we are still within the range of validity of the low Mach number approach. The first calculation incorporates the η_ρ term as introduced in § 2; the second calculation sets this term to zero. (We refer to the latter calculations as the $\eta_\rho \equiv 0$ case.) We use this comparison to isolate the significance of the η_ρ term in the method.
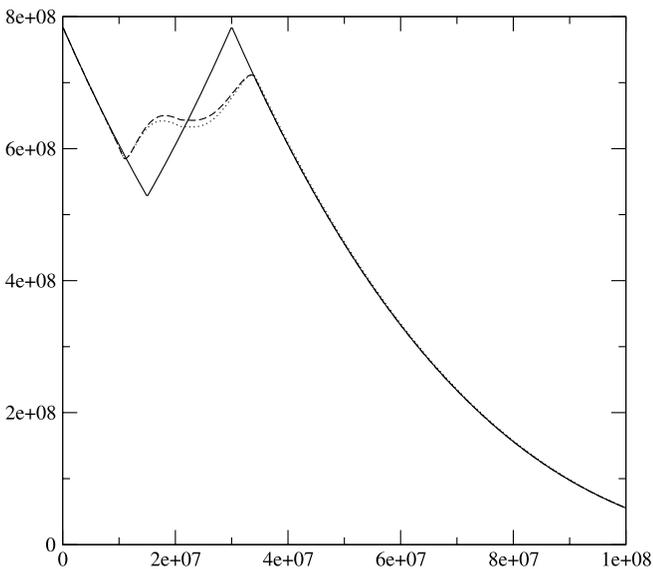
FIG. 8.—Shown here are ρ_0 and $\overline{\rho}$ at $t = 0$ and 0.85 s. The solid curve is $\overline{\rho}$ and ρ_0 at $t = 0$ for both calculations, as well as ρ_0 at $t = 0.85$ s for the calculation with $\eta_\rho \equiv 0$. The dotted curve shows $\overline{\rho}$ as well as ρ_0 at $t = 0.85$ s for the current algorithm; the dashed curve is $\overline{\rho}$ at $t = 0.85$ s for the $\eta_\rho \equiv 0$ case.
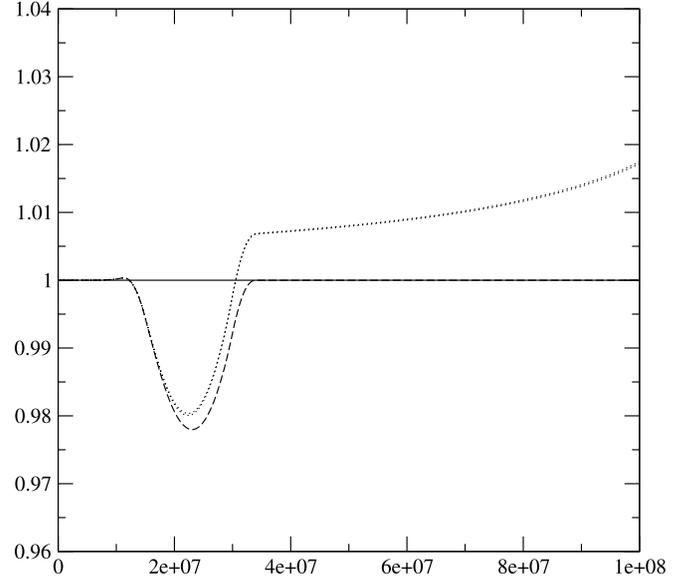
FIG. 9.—Ratio of p_0 and p_{HSE} at $t = 0.85$ s to p_0 at $t = 0$. The solid curve represents p_0 at $t = 0.85$ s for the $\eta_\rho \equiv 0$ case. The dotted curve represents p_0 and p_{HSE} at $t = 0.85$ s for the current algorithm. The dashed curve is p_{HSE} for the calculation with $\eta_\rho \equiv 0$.

In Figure 8 we plot the average density, $\overline{\rho}$, and base state density, ρ_0, at $t = 0$ and 0.85 s for both calculations. We see from this figure that the presence of the η_ρ term successfully enforces that $\rho_0 = \overline{\rho}$ at all times; by contrast, the base state remains unchanged in the $\eta_\rho \equiv 0$ case. We also note that the actual solution (in the form of $\overline{\rho}$) in fact changes when the η_ρ term is included; this difference is visible in the region of convective overturning and is present but difficult to see in the region above the overturning.

In Figure 9 we see the hydrostatic pressure, p_{HSE}, and base state pressure, p_0, at $t = 0$ and 0.85 s. We define p_{HSE} as the discrete integral of $(-\overline{\rho}g)$ from the pressure at the top of the domain downward. The data in Figure 9 are plotted as a ratio relative to the initial base state pressure. We note several things from this figure. First, recalling that p_{HSE} is the integral of $\overline{\rho}$ and $\overline{\rho} = \rho_0$ for the current algorithm, the fact that $p_{\mathrm{HSE}} = p_0$ at $t = 0.85$ s (*dotted curve*) confirms that although the discrete updates of ρ_0 and p_0 do not explicitly maintain hydrostatic equilibrium, the discretization of the update equations is sufficiently accurate that hydrostatic balance, which follows from the analytic form of the equations, is in fact discretely maintained. Second, we note that there is a roughly 2% deviation of the hydrostatic pressure from its initial value in the $\eta_\rho \equiv 0$ case; this time variation is not reflected in p_0. Finally, we observe that in the region above the convective overturning the dashed curve, representing p_{HSE} (calculated from an incorrect $\overline{\rho}$) at $t = 0.85$ s for the $\eta_\rho \equiv 0$ case, matches the original p_0, indicating that the average density and pressure have not evolved in time. Physically, this could only occur if the convective overturning had happened in a region of constant entropy. Thus, we conclude that the fact that p_0 does not represent the average hydrostatic pressure in fact results in a hydrostatic pressure that is physically incorrect.

Finally, we note the magnitude of $(\delta p)_{\mathrm{drift}}$ is comparable for both the current algorithm and the $\eta_\rho \equiv 0$ case and never exceeds approximately 0.1%. This is as expected; as noted above, $(\delta p)_{\mathrm{drift}}$ represents how well the constraint equation (see eq. [12]) constrains the dynamics so that the local thermodynamic pressure is close to p_0 and is independent of how accurately p_0 represents p_{HSE}.

5. CONCLUSIONS

This paper is the third in a set of papers that has demonstrated a new algorithm for evolving low Mach number reacting flows in Type Ia supernovae. In Paper I we demonstrated the accuracy of the low Mach number approach for nonreacting flows, with no base state adjustment, in a stellar atmosphere. In Paper II we extended the methodology to allow for time evolution of the base state in response to significant heating.

In this paper we have modified the evolution equations to allow the base state to evolve in response to large-scale convective motions as well as heat release. We have extended the algorithm to incorporate nuclear chemistry characteristic of the early stages of Type Ia supernovae. We have demonstrated that, in the presence of reactions, we can attain second-order accuracy in the thermodynamic variables. We further demonstrated that our method remains stable over long-timescale evolution of fully convective flow in plane-parallel geometry and that the thermodynamic pressure calculated from the equation of state does in fact remain close to the time-dependent background pressure. The simulation code described here, named MAESTRO, will be our primary tool for exploring the conditions leading up to the explosion of Type Ia supernovae.

Throughout the development of this new algorithm, we have validated the new methodology with detailed comparisons to fully compressible codes. Because of their wide availability and ease of implementation, compressible algorithms are the current workhorse of multidimensional stellar astrophysics. We have shown that the low Mach number algorithm remains stable and captures the essential features of the flow even for Mach numbers in excess of 0.2. Although the low Mach number algorithm is more complicated than compressible algorithms, it reduces the number of time steps needed to reach a particular time by a factor of $\sim 1/M$ relative to compressible codes.

Our next step in the development of this methodology will be to complete the implementation in three dimensions and address the remaining numerical issues needed to model a spherical star in Cartesian geometry. Some initial tests of MAESTRO evolving a full self-gravitating star can be found in Almgren et al. (2007). The main changes required are a different treatment of the hydrostatic adjustment process, taking into account expansion in a self-gravitating star, and a procedure to map the one-dimensional radial base state to and from the Cartesian grid. Further improvements include adaptive mesh refinement and more sophisticated reaction networks. Ultimately, we will augment the present algorithm with methodology for capturing long-wavelength acoustics in order to be able to evolve the flow from the very subsonic regime through Mach numbers close to unity.

APPENDIX A

EVALUATING ξ_k AND p_{X_k}

Adding the reactions to the equation set brings with it two additional thermodynamic quantities that we need to evaluate,

$$\xi_k = \left.\frac{\partial h}{\partial X_k}\right|_{p,T,(X_j, j \neq k)}, \qquad p_{X_k} = \left.\frac{\partial p}{\partial X_k}\right|_{\rho,T,(X_j, j \neq k)}.$$

In evaluating these expressions, it is important to note what is being held constant. The stellar equation of state we use (Timmes & Swesty 2000) is a function of ρ, T, $\bar{A}$, and $\bar{Z}$, where the latter two variables are composition terms,

$$\bar{A} \equiv \left(\sum_k \frac{X_k}{A_k}\right)^{-1}, \qquad \bar{Z} \equiv \bar{A} \sum_k \frac{Z_k X_k}{A_k},$$

where A_k is the atomic mass of species k and Z_k is the charge. The thermodynamic derivatives returned by the equation of state routine are with respect to one of these variables while holding the others fixed. Therefore, we want to express these quantities in terms of derivatives with respect to ρ, T, $\bar{A}$, and $\bar{Z}$. This means that we need to find an alternate expression for ξ_k, so that ρ and T are held constant, rather than p and T, and we need to express both ξ_k and p_{X_k} as derivatives with respect to $\bar{A}$ and $\bar{Z}$.

In deriving the temperature equation, equation (8), we started with the enthalpy, which is the most natural thermodynamic quantity when pressure is one of the independent variables. Here, we want ρ to be an independent variable, so starting with the internal energy, e, is more natural. The internal energy evolution of the system is governed by

$$\rho \frac{De}{Dt} + p \nabla \cdot \boldsymbol{U} = \rho H_{\mathrm{nuc}}, \tag{A1}$$

or, using the mass continuity equation,

$$\rho \frac{De}{Dt} = \frac{p}{\rho} \frac{D\rho}{Dt} + \rho H_{\mathrm{nuc}}. \tag{A2}$$

Now, taking $e = e(\rho, T, X_k)$, we have

$$\frac{De}{Dt} = \frac{\partial e}{\partial T}\bigg|_{\rho, X_k} \frac{DT}{Dt} + \frac{\partial e}{\partial \rho}\bigg|_{T, X_k} \frac{D\rho}{Dt} + \sum_k \frac{\partial e}{\partial X_k}\bigg|_{\rho, T, (X_j, j \neq k)} \frac{DX_k}{Dt}.$$

Identifying the specific heat at constant volume as $c_v = \partial e / \partial T|_{\rho, X_k}$, defining $e_\rho \equiv \partial e / \partial \rho|_{T, X_k}$ and $e_{X_k} \equiv \partial e / \partial X_k|_{\rho, T, (X_j, j \neq k)}$, and using the species conservation equation, this is

$$\frac{De}{Dt} = c_v \frac{DT}{Dt} + e_\rho \frac{D\rho}{Dt} + \sum_k e_{X_k} \dot{\omega}_k.$$

Substituting this into equation (A2), we have

$$\rho c_v \frac{DT}{Dt} = \rho \left(\frac{p}{\rho^2} - e_\rho \right) \frac{D\rho}{Dt} - \sum_k \rho e_{X_k} \dot{\omega}_k + \rho H_{\text{nuc}}. \tag{A3}$$

We can eliminate $D\rho/Dt$ using equation (7), giving

$$\rho \left[c_v + \left(\frac{p}{\rho^2} - e_\rho \right) \frac{p_T}{p_\rho} \right] \frac{DT}{Dt} = \frac{\rho}{p_\rho} \left(\frac{p}{\rho^2} - e_\rho \right) \frac{Dp}{Dt} - \sum_k \rho \left[e_{X_k} + \frac{1}{p_\rho} \left(\frac{p}{\rho^2} - e_\rho \right) p_{X_k} \right] \dot{\omega}_k + \rho H_{\text{nuc}}. \tag{A4}$$

Comparing to equation (8), we see that the specific heats are related via

$$c_p = c_v + \left(\frac{p}{\rho^2} - e_\rho \right) \frac{p_T}{p_\rho}. \tag{A5}$$

The coefficient of the Dp/Dt term gives

$$h_p = \frac{1}{\rho} \left(1 - \frac{p}{\rho p_\rho} \right) + \frac{1}{p_\rho} e_\rho, \tag{A6}$$

which was used in Paper I when computing α. Finally, we have

$$\xi_k = e_{X_k} + \frac{1}{p_\rho} \left(\frac{p}{\rho^2} - e_\rho \right) p_{X_k}, \tag{A7}$$

where all the derivatives on the right-hand side are either at constant T or constant ρ. This is the form we need when computing ξ_k from our equation of state.

As discussed in Dursi & Timmes (2006), we can evaluate the derivatives with respect to the species from the average compositional variables $\bar{A}$ and $\bar{Z}$, using the chain rule, as the equation of state routine does when it returns derivatives with respect to $\bar{A}$ and $\bar{Z}$. We write e_{X_k} and p_{X_k} as

$$p_{X_k} = \frac{\partial p}{\partial \bar{A}}\bigg|_{\rho, T, \bar{Z}} \frac{\partial \bar{A}}{\partial X_k} + \frac{\partial p}{\partial \bar{Z}}\bigg|_{\rho, T, \bar{A}} \frac{\partial \bar{Z}}{\partial X_k} = -\frac{\bar{A}^2}{A_k} \frac{\partial p}{\partial \bar{A}}\bigg|_{\rho, T, \bar{Z}} + \frac{\bar{A}}{A_k} \left(Z_k - \bar{Z} \right) \frac{\partial p}{\partial \bar{Z}}\bigg|_{\rho, T, \bar{A}}, \tag{A8}$$

$$e_{X_k} = \frac{\partial e}{\partial \bar{A}}\bigg|_{\rho, T, \bar{Z}} \frac{\partial \bar{A}}{\partial X_k} + \frac{\partial e}{\partial \bar{Z}}\bigg|_{\rho, T, \bar{A}} \frac{\partial \bar{Z}}{\partial X_k} = -\frac{\bar{A}^2}{A_k} \frac{\partial e}{\partial \bar{A}}\bigg|_{\rho, T, \bar{Z}} + \frac{\bar{A}}{A_k} \left(Z_k - \bar{Z} \right) \frac{\partial e}{\partial \bar{Z}}\bigg|_{\rho, T, \bar{A}}. \tag{A9}$$

Then ξ_k can be evaluated from equation (A7).

APPENDIX B

CONSTRUCTION OF ADVECTIVE VELOCITIES

To construct the advective velocities we first extrapolate only the normal component of $\tilde{U}$ from cell centers at t^n to edges at $t^{n+1/2}$ using a second-order Taylor series expansion in space and time. The time derivative is replaced using equation (37), the evolution equation for $\tilde{U} = (\tilde{u}, \tilde{w})$. In all of the equations below, $w_0 = w_0^{n+1/2, \star}$, $\pi_0 = \pi_0^{(1)}$, and $\tilde{U}^{\text{ADV}, \star} = \tilde{U}^{\text{ADV}, (1), \star}$ for the construction of $\tilde{U}^{\text{ADV}, (1)}$, and $w_0 = w_0^{n+1/2}$, $\pi_0 = \pi_0^{(2)}$, and $\tilde{U}^{\text{ADV}, \star} = \tilde{U}^{\text{ADV}, (2), \star}$ for the construction of $\tilde{U}^{\text{ADV}, (2)}$.

For simplicity we present the construction in two dimensions, although extension to three dimensions is straightforward and is given in detail in Almgren et al. (1998). In the nonradial direction, we have

$$\tilde{u}_{i+1/2, j}^L \approx \tilde{u}_{i,j}^n + \frac{\Delta x}{2} \tilde{u}_x + \frac{\Delta t}{2} \tilde{u}_t$$

$$= \tilde{u}_{i,j} + \left(\frac{\Delta x}{2} - \tilde{u}_{i,j} \frac{\Delta t}{2} \right) \left(\tilde{u}_x^{\lim} \right)_{i,j} - \frac{\Delta t}{2} \left[(\tilde{w} + w_0) \tilde{u}_r \right]_{i,j}^{\text{trans}} - \frac{\Delta t}{2} \left(\frac{1}{\rho^n} G_x \pi^{n-1/2} \right)_{i,j}, \tag{B1}$$

extrapolated from (i,j), and

$$
\begin{aligned}
\tilde{u}^R_{i+1/2,j} &\approx \tilde{u}^n_{i+1,j} - \frac{\Delta x}{2}\tilde{u}_x + \frac{\Delta t}{2}\tilde{u}_t \\
&= \tilde{u}_{i+1,j} + \left(-\frac{\Delta x}{2} - \tilde{u}_{i+1,j}\frac{\Delta t}{2}\right)\left(\tilde{u}^{\lim}_x\right)_{i+1,j} - \frac{\Delta t}{2}[(\tilde{w}+w_0)\tilde{u}_r]^{\mathrm{trans}}_{i+1,j} - \frac{\Delta t}{2}\left(\frac{1}{\rho^n}G_x\pi^{n-1/2}\right)_{i+1,j},
\end{aligned}
\tag{B2}
$$

extrapolated from $(i+1,j)$.

In evaluating these terms, the first derivatives normal to the face (in this case $\tilde{u}^{\lim}_x$) are evaluated using a monotonicity-limited fourth-order slope approximation (Colella 1985). The construction of the transverse derivative terms ($[(\tilde{w}+w_0)\tilde{u}_r]^{\mathrm{trans}}$ in this case) is described in detail in Almgren et al. (1998). The pressure gradient terms use a discretization of the gradient operator, $\boldsymbol{G} = (G_x, G_r)$, which defines a cell-centered gradient from a node-based pressure field; this is the same gradient operator used in the final projection in step 11.

Analogous formulae are used to predict values for $\tilde{w}^{T/B}_{i,j+1/2}$,

$$
\begin{aligned}
\tilde{w}^B_{i,j+1/2} &\approx \tilde{w}^n_{i,j} + \frac{\Delta r}{2}\tilde{w}_r + \frac{\Delta t}{2}\tilde{w}_t \\
&= \tilde{w}_{i,j} + \left[\frac{\Delta r}{2} - (\tilde{w}+w_0)_{i,j}\frac{\Delta t}{2}\right]\left(\tilde{w}^{\lim}_r\right)_{i,j} - \frac{\Delta t}{2}\left(\tilde{u}\tilde{w}_x\right)^{\mathrm{trans}}_{i,j} \\
&\quad - \frac{\Delta t}{2}\left\{[\tilde{w}(w_0)_r]_{i,j} - \left(\frac{1}{\rho}G_r\pi^{n-1/2}\right)_{i,j} + \left(\frac{1}{\rho^n_0}G_r\pi_0\right)_{i,j} + \left(\frac{\rho^n - \rho^n_0}{\rho^n}g\right)_{i,j}\right\},
\end{aligned}
\tag{B3}
$$

extrapolated from (i,j), and

$$
\begin{aligned}
\tilde{w}^T_{i,j+1/2} &\approx \tilde{w}^n_{i,j+1} - \frac{\Delta r}{2}\tilde{w}_r + \frac{\Delta t}{2}\tilde{w}_t \\
&= \tilde{w}_{i,j+1} + \left[-\frac{\Delta r}{2} - (\tilde{w}+w_0)_{i,j+1}\frac{\Delta t}{2}\right]\left(\tilde{w}^{\lim}_r\right)_{i,j+1} - \frac{\Delta t}{2}\left(\tilde{u}\tilde{w}_x\right)^{\mathrm{trans}}_{i,j+1} \\
&\quad - \frac{\Delta t}{2}\left\{[\tilde{w}(w_0)_r]_{i,j+1} - \left(\frac{1}{\rho}G_r\pi^{n-1/2}\right)_{i,j+1} + \left(\frac{1}{\rho^n_0}G_r\pi_0\right)_{i,j+1} + \left(\frac{\rho^n - \rho^n_0}{\rho^n}g\right)_{i,j+1}\right\},
\end{aligned}
\tag{B4}
$$

extrapolated from $(i,j+1)$.

Upwinding is used to determine $\tilde{\boldsymbol{U}}^{\mathrm{ADV},\star}$ at each edge as

$$
\tilde{u}^{\mathrm{ADV},\star}_{i+1/2,j} = \begin{cases}
\frac{1}{2}\left(\tilde{u}^L_{i+1/2,j} + \tilde{u}^R_{i+1/2,j}\right), & \tilde{u}^L_{i+1/2,j} + \tilde{u}^R_{i+1/2,j} = 0 \text{ or } \tilde{u}^L_{i+1/2,j} < 0,\ \tilde{u}^R_{i+1/2,j} > 0, \\
\tilde{u}^L_{i+1/2,j}, & \tilde{u}^L_{i+1/2,j} + \tilde{u}^R_{i+1/2,j} > 0, \\
\tilde{u}^R_{i+1/2,j}, & \tilde{u}^L_{i+1/2,j} + \tilde{u}^R_{i+1/2,j} < 0,
\end{cases}
$$

and similarly for defining $\tilde{w}^{\mathrm{ADV},\star}_{i,j+1/2}$. For the construction of $\tilde{\boldsymbol{U}}^{\mathrm{ADV},(1)}$, we enforce the divergence constraint by solving

$$
D^{\mathrm{MAC}}\left(\frac{\beta^n_0}{\rho^n}\boldsymbol{G}^{\mathrm{MAC}}\phi^{\mathrm{MAC},(1)}\right) = D^{\mathrm{MAC}}\left(\beta^n_0\tilde{\boldsymbol{U}}^{\mathrm{ADV},(1),\star}\right) - \beta^n_0\left(S^{n+1/2,\star} - \overline{S}^{n+1/2,\star}\right)
\tag{B5}
$$

for ϕ, where D^{MAC} represents a centered approximation to a cell-based divergence from edge-based velocities and $\boldsymbol{G}^{\mathrm{MAC}}$ represents a centered approximation to edge-based gradients from cell-centered data. We solve the linear system from equation (B5) using multigrid V-cycles with Gauss-Seidel red-black relaxation. The provisional advective velocity, $\tilde{\boldsymbol{U}}^{\mathrm{ADV},(1)}$, is then

$$
\tilde{\boldsymbol{U}}^{\mathrm{ADV},(1)} = \tilde{\boldsymbol{U}}^{\mathrm{ADV},(1),\star} - \frac{1}{\rho^n}\boldsymbol{G}^{\mathrm{MAC}}\phi^{\mathrm{MAC},(1)},
\tag{B6}
$$

which satisfies

$$
D^{\mathrm{MAC}}\left(\beta^n_0\tilde{\boldsymbol{U}}^{\mathrm{ADV},(1)}\right) = \beta^n_0\left(S^{n+1/2,\star} - \overline{S}^{n+1/2,\star}\right),
\tag{B7}
$$

the discrete form of equation (39).

For the construction of $\tilde{\boldsymbol{U}}^{\mathrm{ADV},(2)}$, we enforce the divergence constraint by solving

$$
D^{\mathrm{MAC}}\left(\frac{\beta^{n+1/2,\star}_0}{\rho^{n+1/2,\star}}\boldsymbol{G}^{\mathrm{MAC}}\phi^{\mathrm{MAC},(2)}\right) = D^{\mathrm{MAC}}\left(\beta^{n+1/2,\star}_0\tilde{\boldsymbol{U}}^{\mathrm{ADV},(2),\star}\right) - \beta^{n+1/2,\star}_0\left(S^{n+1/2} - \overline{S}^{n+1/2}\right),
\tag{B8}
$$

where $\rho^{n+1/2,\star} = (\rho^n + \rho^{n+1,\star})/2$ and $\beta_0^{n+1/2,\star} = (\beta_0^n + \beta_0^{n+1,\star})/2$. The final advective velocity is then

$$\tilde{U}^{\mathrm{ADV},(2)} = \tilde{U}^{\mathrm{ADV},(2),\star} - \frac{1}{\rho^{n+1/2,\star}} G^{\mathrm{MAC}} \phi^{\mathrm{MAC},(2)}, \tag{B9}$$

which satisfies

$$D^{\mathrm{MAC}}\left(\beta_0^{n+1/2,\star} \tilde{U}^{\mathrm{ADV},(2)}\right) = \beta_0^{n+1/2,\star}\left(S^{n+1/2} - \overline{S}^{n+1/2}\right). \tag{B10}$$

APPENDIX C

COMPUTING β_0

A high-order reconstruction of the integrand in the β_0 integral (see eq. [13]) improves the overall solution relative to a lower order reconstruction. Here we outline the integration procedure using piecewise linear reconstruction of the state variables. We wish to compute

$$\beta_0(r,t) = \beta_0(0,t) \exp\left(\int_0^r \frac{1}{\overline{\Gamma}_1 p_0} \frac{\partial p_0}{\partial r'} dr'\right).$$

We split the integral such that we integrate from the low edge of each cell to the high edge, resulting in edge-centered values of β_0. The initial value of β_0 on the lowest edge of the domain will be assigned the value $\beta_{01/2} = \rho_{01}$. Letting i be the index in the radial direction, we define β_0 on the high edge of cell i using

$$\beta_{0i+1/2} = \beta_{01/2} \exp\left[-\sum_{j=1}^{i} \int_{r_{j-1/2}}^{r_{j+1/2}} \frac{\rho_0(r')|g(r')|}{\overline{\Gamma}_1(r')p_0(r')} dr'\right] = \beta_{01/2} \prod_{j=1}^{i} \exp\left[-\int_{r_{j-1/2}}^{r_{j+1/2}} \frac{\rho_0(r')|g(r')|}{\overline{\Gamma}_1(r')p_0(r')} dr'\right]. \tag{C1}$$

We note that in a plane-parallel setting, $g(r)$ is constant, but for a spherical star we must compute $g(r)$ from $\rho_0(r)$ before beginning the above integration.

Beginning with $\beta_{01/2}$, we integrate over the first cell ($i = 1$) to define $\beta_{03/2}$ and continue integrating cell-by-cell. We use piecewise linear reconstruction of ρ_0, $\overline{\Gamma}_1$, and p_0,

$$\rho_0(r) = \rho_{0j} + \lambda_j(r - r_j), \qquad \overline{\Gamma}_1(r) = \overline{\Gamma}_{1j} + \mu_j(r - r_j), \qquad p_0(r) = p_{0j} + \nu_j(r - r_j).$$

Here, the average value of each quantity is just the zonal value, and the slopes (λ, μ, and ν) are computed as slope-limited centered differences. We can now compute the integral

$$I_j \equiv |g(r_j)| \int_{r_j - \Delta r/2}^{r_j + \Delta r/2} \frac{\rho_0(r')}{\overline{\Gamma}_1(r')p_0(r')} dr' = |g(r_j)| \int_{r_j - \Delta r/2}^{r_j + \Delta r/2} \frac{\rho_{0j} + \lambda_j(r' - r_j)}{\left[\overline{\Gamma}_{1j} + \mu_j(r' - r_j)\right]\left[p_{0j} + \nu_j(r' - r_j)\right]} dr'.$$

Using a table of integrals, this evaluates to

$$I_j = \frac{|g(r_j)|}{\nu_j \overline{\Gamma}_{1j} - \mu_j p_{0j}} \left[\left(\frac{\lambda_j \overline{\Gamma}_{1j}}{\mu_j} - \rho_{0j}\right) \ln\left(\frac{\overline{\Gamma}_{1j} + \mu_j \Delta r/2}{\overline{\Gamma}_{1j} - \mu_j \Delta r/2}\right) - \left(\frac{\lambda_j p_{0j}}{\nu_j} - \rho_{0j}\right) \ln\left(\frac{p_{0j} + \nu_j \Delta r/2}{p_{0j} - \nu_j \Delta r/2}\right)\right]. \tag{C2}$$

The interface values of β_0 are then evaluated as

$$\beta_{0i+1/2} = \beta_{01/2} \prod_{j=1}^{i} \exp\{-I_j\}.$$

Cell-centered values of β_0 are found by simple averaging,

$$\beta_{0i} = \frac{\beta_{0i-1/2} + \beta_{0i+1/2}}{2}.$$

REFERENCES

Alastuey, A., & Jancovici, B. 1978, ApJ, 226, 1034
Almgren, A. 2000, J. Atmos. Sci., 57, 995
Almgren, A. S., Bell, J. B., Colella, P., Howell, L. H., & Welcome, M. 1998, J. Comput. Phys., 142, 1
Almgren, A. S., Bell, J. B., & Crutchfield, W. Y. 2000, SIAM J. Sci. Comput., 22, 1139
Almgren, A. S., Bell, J. B., Rendleman, C. A., & Zingale, M. 2006a, ApJ, 637, 922 (Paper I)
———. 2006b, ApJ, 649, 927 (Paper II)
Almgren, A. S., Bell, J. B., & Szymczak, W. G. 1996, SIAM J. Sci. Comput., 17, 358
Almgren, A. S., Bell, J. B., & Zingale, M. 2007, J. Phys. Conf. Ser., 78, 012085

Baraffe, I., Heger, A., & Woosley, S. E. 2004, ApJ, 615, 378
Bell, J. B., Day, M. S., Rendleman, C. A., Woosley, S. E., & Zingale, M. A. 2004, J. Comput. Phys., 195, 677
Bell, J. B., & Marcus, D. L. 1992, J. Comput. Phys., 101, 334
Brown, P. N., Byrne, G. D., & Hindmarsh, A. C. 1989, SIAM J. Sci. Stat. Comput., 10, 1038
Caughlan, G. R., & Fowler, W. A. 1988, At. Data Nucl. Data Tables, 40, 283, http://www.phy.ornl.gov/astrophysics/data/cf88/index.html
Colella, P. 1985, SIAM J. Sci. Stat. Comput., 6, 104
———. 1990, J. Comput. Phys., 87, 171
Durran, D. 1990, Meteorol. Monogr., 23, 59
Dursi, L. J., & Timmes, F. X. 2006, ApJ, 641, 1071
Fryxell, B., et al. 2000, ApJS, 131, 273
García-Senz, D., & Bravo, E. 2005, A&A, 430, 585
Graboske, H. C., Dewitt, H. E., Grossman, A. S., & Cooper, M. S. 1973, ApJ, 181, 457
Hillebrandt, W., & Niemeyer, J. C. 2000, ARA&A, 38, 191
Höflich, P., & Stein, J. 2002, ApJ, 568, 779
Hujeirat, A., Thielemann, F., Dusek, J., & Nusser, A. 2007, preprint (arXiv: 0712.3663)

Itoh, N., Totsuji, H., Ichimaru, S., & Dewitt, H. E. 1979, ApJ, 234, 1079
Kuhlen, M., Woosley, S. E., & Glatzmaier, G. A. 2006, ApJ, 640, 407
Lin, D. J., Bayliss, A., & Taam, R. E. 2006, ApJ, 653, 545
Livne, E., Asida, S. M., & Höflich, P. 2005, ApJ, 632, 443
Nicoud, F. 2000, J. Comput. Phys., 158, 71
Niemeyer, J. C., Hillebrandt, W., & Woosley, S. E. 1996, ApJ, 471, 903
Plewa, T., Calder, A. C., & Lamb, D. Q. 2004, ApJ, 612, L37
Röpke, F. K., Hillebrandt, W., Niemeyer, J. C., & Woosley, S. E. 2006, A&A, 448, 1
Röpke, F. K., Woosley, S. E., & Hillebrandt, W. 2007, ApJ, 660, 1344
Sussman, M. M., Almgren, A. S., Bell, J. B., Colella, P., Howell, L., & Welcome, M. 1999, J. Comput. Phys., 148, 81
Timmes, F. X., & Arnett, D. 1999, ApJS, 125, 277
Timmes, F. X., & Swesty, F. D. 2000, ApJS, 126, 501
Weaver, T. A., Zimmerman, G. B., & Woosley, S. E. 1978, ApJ, 225, 1021
Woosley, S. E., Wunsch, S., & Kuhlen, M. 2004, ApJ, 607, 921
Wunsch, S., & Woosley, S. E. 2004, ApJ, 616, 1102
Zingale, M., et al. 2002, ApJS, 143, 539